Interpretation®

Organic content and maturation effects on elastic properties of source rock shales in the Central North Sea

Journal:	*Interpretation*
Manuscript ID	INT-2018-0105.R2
Manuscript Type:	Technical Paper (if no special section applies)
Date Submitted by the Author:	n/a
Complete List of Authors:	Hansen, Jørgen; Universitetet i Oslo Det Matematisk-naturvitenskapelige Fakultet, Dept. of Geosciences Mondol, Nazmul; Universitetet i Oslo Det Matematisk-naturvitenskapelige Fakultet, Dept. of Geosciences; Norges Geotekniske Institutt, Division of Petroleum Geomechanics and Geophysics Fawad, Manzar; Universitetet i Oslo Det Matematisk-naturvitenskapelige Fakultet, Dept. of Geosciences
Keywords:	rock physics, shale, seismic attributes, integration, North Sea
Subject Areas:	Amplitudes, attributes, and subsurface properties

SCHOLARONE™ Manuscripts

ORGANIC CONTENT AND MATURATION EFFECTS ON ELASTIC PROPERTIES OF SOURCE ROCK SHALES IN THE CENTRAL NORTH SEA

Shortened title: Elastic properties of source rock shales

Authors:

Jørgen André Hansen, University of Oslo, Oslo, Norway. E-mail: j.a.hansen@geo.uio.no

Nazmul Haque Mondol, University of Oslo, Oslo, Norway and Norwegian Geotechnical Institute (NGI), Oslo, Norway. E-mail: nazmulh@geo.uio.no

Manzar Fawad, University of Oslo, Oslo, Norway. E-mail: manzar.fawad@geo.uio.no

For Peer Review

Original date of submission: 8. June 2018

Part of this paper has been presented during the 80th EAGE Conference and Exhibition in Copenhagen, June 2018 (DOI: 10.3997/2214-4609.201800865).

ABSTRACT

We investigate the effects of organic content and maturation on the elastic properties of source rock shales, mainly through integration of a well log database from the Central North Sea and associated geochemical data. Our aim is to improve the understanding of how seismic properties change in source rock shales due to geological variations and how these might manifest on seismic data in deeper, undrilled parts of basins in the area. The Tau and Draupne Formations (Kimmeridge Shale equivalents) in immature to early mature stages exhibit variation mainly related to compaction and TOC content. We assess the link between depth, acoustic impedance (AI) and TOC in this setting, and express it as an empirical relation for TOC prediction. Additionally, where shear wave information is available, we combine two seismic properties and infer rock physics trends for semi-quantitative prediction of TOC from V_p/V_s and AI. Furthermore, data from one reference well penetrating mature source rock in the southern Viking Graben indicates that a notable hydrocarbon-effect can be observed as an addition to the inherently low kerogen-related velocity and density. Published Kimmeridge Shale ultrasonic measurements from 3.85 to 4.02 km depth closely coincide with well log measurements in the mature shale, indicating that upscaled log data is reasonably capturing variations in the actual rock properties. AVO inversion attributes should in theory be interpreted successively in terms of compaction, TOC, and maturation with associated generation of hydrocarbons. Our compaction-consistent decomposition of these effects can be of aid in such interpretations.

For Peer Review

INTRODUCTION

In recent years, research on characterization of source rock shales has become more frequent due to the value of exploiting unconventional shale reservoirs (e.g., Passey et al., 1990; Vernik and Landis, 1996; Passey et al., 2010; Vernik and Milovac, 2011; Alfred and Vernik, 2012; Zhu et al., 2012; Sayers, 2013a; b; Yenugu and Vernik, 2015; Zhao et al., 2018). However, the understanding and theories developed are in principle equally applicable for characterization of organic-rich shales as conventional hydrocarbon source rocks. Source rock maturity is a critical factor in the Central North Sea petroleum system (NPD, 2017). As the source rock maximum burial depth is relatively shallow compared to the peak oil window, localized and/or limited generation of hydrocarbons has been proposed (Ritter, 1988). To identify extent of mature source rock in an area and evaluate possible migration pathways, a good understanding of lateral variations in source rock properties is valuable. For examining source rock properties across larger, less frequently drilled areas, the use of seismic data is required. This process begins with a proper understanding of how organic content and subsequent thermal maturation affects the elastic properties of the rock. Consequently, the motivation for this study is to investigate the effects and relative impact of compaction, organic content and hydrocarbon generation on the elastic properties of organic-rich shales using actual measured data. The goal is to characterize source rock shales in terms of TOC and thermal maturity from seismic data, as well as the associated uncertainties.

Multiple studies assess and predict the petrophysical and elastic properties of organic-rich shales with focus on variations in kerogen content, fluid content, mineralogy, microstructure, texture and anisotropy from a rock physics modeling perspective, mainly aimed at unconventional reservoirs (e.g., Passey et al., 1990; Vernik and Landis, 1996; Sondergeld and Rai, 2011; Vernik and Milovac, 2011; Alfred and Vernik, 2012; Zhu et al.,

For Peer Review

2012; Guo et al., 2013; Sayers, 2013a; b; Yenugu and Vernik, 2015; Zhao et al., 2016). Others focus directly on seismic characterization of organic-rich shales and TOC (Løseth et al., 2011; Badics et al., 2015). However, relatively few contend with the effects of maturation (Avseth and Carcione, 2015; Carcione and Avseth, 2015; Zhao et al., 2016) or incorporate significant amounts of measured data. One of the main challenges with assessing maturation of organic-rich shales when buried to depths and temperatures associated with hydrocarbon generation, is to separate the effects of different factors determining effective shale properties and processes occurring at these conditions.

Firstly, shales are characterized by an assembly of clay minerals (mainly illite, smectite, kaolinite and chlorite), as well as silt- and sand sized grains (quartz, feldspar), pyrite, and carbonates (e.g. dolomite, calcite and siderite). Organic-rich shales additionally contain a certain amount of organic matter in the form of kerogen, bitumen and volatile hydrocarbons, expressed by TOC (Total Organic Carbon) in weight-percent. TOC commonly ranges from 2–3 wt. % to more than 20 wt. % (Vernik and Landis, 1996; Gautier, 2005). General characteristic features are uniquely high gamma ray signature, low sonic velocity and density, and a strong intrinsic anisotropy compared to non-organic equivalent shales due to the presence of laminated or patchy low density and low velocity kerogen (Vernik and Landis, 1996).

Secondly, as temperatures reach approximately 70–80°C, transformation of thermodynamically unstable smectite minerals to illite will occur in the presence of a potassium source (Bjørlykke, 1998; Peltonen et al., 2009; Thyberg and Jahren, 2011; Kalani et al., 2015a; Zadeh et al., 2016). This process also releases water and precipitates microquartz out of solution which may act as cement, or distribute in a sheet-like manner at elevated temperature above 90–100°C. Quartz cement will increase the stiffness of the rock

For Peer Review

framework, which increases sonic velocity. Cement may also increase the intrinsic anisotropy of the shales if precipitated parallel to the bedding/laminated clay texture (Thyberg and Jahren, 2011). Water released during this process can contribute to overpressure in the pores (i.e., reduction of sonic velocity and an appearance of higher porosity) due to the generally low permeability of shales. Similar processes occur during kaolinite–illite transformation at more than ~130°C (Bjørlykke, 1998; Zadeh et al., 2016).

Thirdly, at temperatures higher than ~90°C, maturation of solid kerogen results in generation of hydrocarbons in the organic matter pore space. Converting relatively denser kerogen to oil or gas will similarly increase the pore pressure (i.e., lead to overpressure), and in matured source rocks that have passed through mainstage hydrocarbon generation and sufficient amounts have been generated, microfractures are expected to occur (Vernik, 1994; Kalani et al., 2015b). Earlier formation of horizontal microcracks has also been demonstrated in tight, strongly laminated, organic-rich shale with abundant flattened kerogen accumulations (Lash and Engelder, 2005). Thermal maturation also directly affects the elastic properties of kerogen, since maturation involves formation of organic pores within the solid kerogen. The density of the remaining kerogen increases because the carbon fraction increases relative to hydrogen (Alfred and Vernik, 2012; Yenugu and Vernik, 2015; Dang et al., 2016; Ibrahim and Mukerji, 2017).

Initially in our study, we calculate continuous TOC logs in all wells and examine maturation parameters from geochemical laboratory studies. Secondly, we review the relationship between a single seismic property (acoustic impedance) and source rock properties in the study area. Furthermore, we incorporate additional attributes and background templates in more comprehensive rock physics crossplots to observe behavior

For Peer Review

related to 1) compaction, 2) organic content and 3) hydrocarbon effects. Finally, AVO signatures are predicted and subsequent classification is discussed briefly.

GEOLOGICAL SETTING AND LITHOSTRATIGRAPHY

The Central North Sea has experienced two important rifting episodes (Late Paleozoic and Late Jurassic–Early Cretaceous) resulting in a large number of structural elements (Faleide et al., 2008). Uplift and erosion in multiple phases, as recent as Neogene, have had laterally varying effects across the region (Hansen et al., 2017). Additionally, Triassic and Early Jurassic sediments are absent in certain areas due to Early Jurassic uplift of the Mid North Sea Dome causing erosion and nondeposition (Ziegler, 1992; Mannie et al., 2014).

The study area described in terms of structural elements incorporates the Ling Depression, parts of the Åsta Graben, and the Egersund Basin, which are sub-elements within the Norwegian-Danish Basin, located in the Central North Sea (Figure 1). These basin areas surround the Sele High, and are bounded by the Stavanger Platform to the east towards the Norwegian mainland, the Jæren High and Sørvestlandet High to the west and southwest towards the Central Graben, and the Utsira High and Viking Graben to the north and northwest. The northeast Ling Depression/Åsta Graben is the least explored area compared to the Egersund Basin or the southwest Ling Depression based on the density of exploration wells (Figure 1). Oil and gas fields shown in grey in Figure 1 indicate prolific areas to the north and west (Utsira High, Viking Graben).

In this study we investigate two Upper Jurassic organic-rich shale formations, equivalent to the Kimmeridge Shale (UK), namely the Draupne Formation (part of the Viking Group) which is present in the southwestern part of the Ling Depression, and the Tau Formation (part of the Boknfjord Group) in the northeastern part of the Ling Depression, the

For Peer Review

Åsta Graben and the Egersund Basin (Figure 2). Both the Draupne and Tau Formations are black shales considered to be rich potential source rocks for hydrocarbons, with typically 5–12 wt. % TOC and HI up to 700 mg HC/g TOC at immature stage, if subjected to sufficient temperature (Pedersen et al., 2006). Adjacent formations Sauda, Egersund and Heather also have source rock potential, but the quality is generally poorer and more variable, and these are not directly considered in our study. The Boknfjord and Viking Groups form primary seals for Jurassic sandstone reservoirs of the Vestland Group (Bryne/Sandnes and Sleipner/Hugin Formations, respectively) along with the overlying shale dominated Cromer Knoll Group.

DATABASE AND METHODS

We compiled a well database consisting of twenty-one (21) exploration wells based on availability, location, negligible deviation, and presence of relevant data (Figure 1). All wells contain standard well log measurements such as gamma ray, bulk density (ρ_b), resistivity, and P-wave velocity (V_p), but only seven (7) wells contain S-wave velocity (V_s). As part of the initial data conditioning and quality control, due to exhumation in parts of the study area, we estimate maximum burial depth for each well location by comparing velocity-depth trends to experimental compaction trends (Mondol, 2009; Kalani et al., 2015a; Hansen et al., 2017). Relevant geochemical data such as TOC, T_{max}, hydrogen index (HI) and vitrinite reflectance (R_o) measured on rock samples are obtained from reports in the public domain provided by the Norwegian Petroleum Directorate (NPD, 2017). Key information about each well is summarized in Table 1. Supplementary data regarding lithology and mineralogical composition relies on well completion reports and previously published literature (Kalani et al., 2015b; Zadeh et al., 2017). Furthermore, we have re-digitized a dataset from Sondergeld

For Peer Review

et al. (2000) with laboratory measurements of anisotropic elastic properties (V_p, V_s, ρ_b, and Thomsen anisotropy parameters) from the Kimmeridge shale subjected to 20 MPa effective pressure. These data are not depth-indexed, but represent samples from between approximately 3.85–4.02 km depth.

In terms of seismic coverage, no prestack seismic data is available for this study. One poststack seismic cube is available from the northeast Ling Depression (Figure 1). A network of 2D seismic lines provided regional scale interpretations of key horizons.

For Peer Review

Geochemical data and TOC prediction

Based on the geochemical data we can directly obtain an overview of maturity trends, kerogen typing and organic content variations. Poor quality vitrinite reflectance readings are excluded. Interpretation is supported by crossplots of T_{max} versus hydrogen index (HI) and TOC versus HI. In the next step, all wells are populated with continuous calculated TOC in the organic rich shale interval, calibrated to sample measurements. Relatively recently drilled wells with V_s do not typically contain geochemical calibration data, so strategic selection of wells is necessary to allow neighboring wells to serve as calibration for predicting TOC. The commonly used ΔlogR method using sonic and resistivity logs (Meyer and Nederlof, 1984; Passey et al., 1990) was tested, but a relation between TOC in weight percent and bulk density (Equation 1) appear to provide more consistent predictions in the investigated wells when compared to TOC from core/cuttings (Figure 3). TOC from density (Vernik and Landis, 1996; Carcione, 2000) is calculated as

$$\text{TOC (wt. \%)} = a\,[\rho_k(\rho_m - \rho_b)] / [\rho_b(\rho_m - \rho_k)]. \qquad (1)$$

Here, ρ_k is kerogen density which has a range of 1.1–1.6 g/cm^3, and is dependent on maturity (Vernik and Landis, 1996; Passey et al., 2010; Vernik and Milovac, 2011; Alfred and Vernik, 2012; Dang et al., 2016). ρ_m is matrix density, which in reality varies according to mineralogy and diagenesis, i.e., clay mineral transformation (Carcione and Avseth, 2015). ρ_b is the bulk density log measurement, and a is a constant related to the fraction of carbon in organic matter and can vary according to maturation level. For instance, $a = 67$ is assumed by Vernik and Landis (1996), whereas $a = 70–85$ is suggested by Vernik and Milovac (2011). ρ_k, ρ_m, and a in our calculations are determined by obtaining an optimal fit with measured TOC on cores and cuttings from geochemical reports (NPD, 2017). Equation 1 is strictly valid for shales with negligible porosity effects on the bulk density measurement, which we assume for immature source rocks, but can be adjusted to obtain an acceptable fit with mature source rock as well, given calibration data.

Reviewing acoustic impedance from well logs and seismic inversion

Next, we investigate how acoustic impedance (AI) varies with burial depth and rock properties across the study area. Data coverage is quite extensive, comprising the complete well log database and a poststack seismic cube. After interpreting key horizons on the seismic volume, we perform a colored inversion and a model-based inversion for relative AI and absolute AI, respectively. The purpose is to qualitatively analyze lateral and vertical variations in AI within the scope of this study, rather than to perform high-detail quantitative interpretations of these results.

Establishing trends using multiple seismic properties

Furthermore, we aim for meaningful predictions of how the target properties influence combinations of seismic attributes, e.g., velocity ratio (V_p/V_s), AI and the Lamé petrophysical parameters $\lambda\rho$ and $\mu\rho$. Consequently, for the following part of the study we focus on the seven

For Peer Review

wells containing shear velocity measurements (Table 1). Three of these wells are located in the southwest Ling Depression, one in the northeast Ling Depression, two in the Egersund Basin, and one in the southern Viking Graben (Figure 1). We primarily analyze a standard rock physics crossplot, V_p/V_s versus AI, in order to establish a link between seismic data and geological variations in our observations. For completeness, behavior in the λ–μ–ρ (LMR) domain is also considered. Data are examined both on the recorded resolution of well log measurements, and after applying upscaling (blocking) to approximate what we can expect to resolve with seismic. Using upscaled logs (20 measurement steps ≈ 3 m averaging intervals) can be advantageous for observing variations less obscured by high-frequency scatter and to mimic seismic resolution (Avseth and Carcione, 2015), yet a disadvantage is loss of detail from the high-resolution well log data.

For our purpose, constructing a rock physics template (Ødegaard and Avseth, 2004) to serve as a reference for the area is useful. Firstly, in place of a theoretical model, a background compaction trend is established in the V_p/V_s–AI crossplot with well log data from shale dominated formations with negligible organic content at different depths across the area. The considered formations are proximal in depth to the Tau and Draupne Formations, and are assumed to represent a local reference for compaction as a function of depth within non-source clay dominated rocks. For context, we compare to a more general inorganic brine-saturated shale trend utilized and discussed in previous publications (Avseth and Carcione, 2015, originally from Khadeeva and Vernik, 2014). Secondly, a brine saturated sandstone trend is calculated (modified Hashin-Shtrikman upper bound interpolation and Gassmann theory) and calibrated to well log data in predominantly clean sandstones, and a gas saturated sandstone trend is predicted using Gassmann fluid substitution. The behavior of organic-rich

For Peer Review

shales in the area can subsequently be compared to these trends, which provide better control of the previously mentioned changes that occur related to progressive burial and compaction.

We consider data from six wells in the Ling Depression and Egersund Basin, in locations where maturation is limited (Table 2; Ritter, 1988), to investigate the effect of TOC on the elastic properties. We also employ a kerogen substitution method to complement our interpretations and support the proposed trends (Vernik, 2016). A limitation for using the model is that we necessarily have to generalize mineralogical fractions (Kalani et al., 2015b), and estimate non-kerogen and kerogen properties using standard values, since which we currently lack explicit measurements. Kerogen density is approximated from vitrinite reflectance with the empirical relation suggested by Alfred and Vernik (2012),

$$\rho_k = 1.293\ R_o^{0.2}\ . \tag{2}$$

In addition to the wells from areas with limited maturation, we have data from one well (15/3-8) representing deeply buried source rock from a proven mature area. Although it serves as a limited sample, it allows us to investigate discrepancies related to hydrocarbons (using well 15/3-1S as geochemical proxy, see also Isaksen and Ledje, 2001). Data adapted from Sondergeld et al. (2000) is used as a secondary comparison to source rocks buried to depths normally associated with advanced maturation. Lucier et al. (2011) utilize Gassmann fluid replacement modeling to obtain reasonable gas-corrected velocities for an upper Jurassic shale gas play in the US, compared to representative organic-lean, brine saturated mudrock trends. After careful consideration of the assumptions behind Gassmann fluid substitution, they argue that it can be applied to shale under certain circumstances, even though quantitative saturation interpretations are likely to be inaccurate. ~~In appropriate circumstances, the rock should firstly be well compacted in order to assume an elastic response to wave propagation, and consequently also support the validity of effective~~

For Peer Review

~~medium modeling (e.g. Hashin-Shtrickman) to approximate a monomineralic rock. The shale must be reasonable to assume as transversely isotropic, so that the symmetry axis aligns with the direction of sonic measurements, thereby approximating the assumption of isotropy (). The assumption of homogeneity is not fulfilled, but is found by to have minor influence for rocks with porosity higher than 5%.~~

In order to do a simple test of the proposition that hydrocarbons have directly influenced the properties of the Draupne Formation in well 15/3-8 (and similarly the ultrasonic measurements of Sondergeld et al., 2000), a fluid substitution from in-situ oil to water was conducted using an average expression of the V_p, V_s and ρ for the upper Draupne shale. The mineralogical composition was approximated from XRD analysis of the Draupne Formation by Zadeh et al. (2017). Mineral moduli and densities were obtained from Mondol et al. (2008) and Avseth and Carcione (2015).

AVO modeling

In order to examine the expected AVO signature of the organic-rich shales at different TOC levels and burial depths, synthetic AVO seismograms are generated using the Aki and Richards (1980) approximation and a linearized Ricker wavelet (length 180 ms, 30 Hz dominant frequency). This simplified wavelet is used for all seven wells, and is designed to closely resemble a statistical wavelet extracted from the poststack 3D seismic cube in the area. The in-situ synthetic responses are subsequently classified in terms of intercept and gradient (I–G), or reflection coefficient as a function of incidence angle (Castagna and Swan, 1997).

RESULTS

For Peer Review

To provide an overview of the extent and depth variations (in TWT), Figure 4a shows top source rock surfaces (both Tau and Draupne Formations) interpreted on 2D seismic data. The lateral extents of these two formations are primarily based on information from the NPD (Norwegian Petroleum Directorate). Note that this map shows present burial depth, meaning that exhumation is not accounted for. In well log data presented below, we have corrected for estimated maximum burial depth (Table 1). The exhumation magnitude is assumed negligible in the westernmost part of the study area (Quadrant 15), and generally increases towards the Norwegian mainland in the east and northeast (e.g., Japsen, 1998; Kalani et al., 2015a; Zadeh et al., 2016; Hansen et al., 2017).

For Peer Review

TOC distribution and thermal maturity indicators

Figure 4b shows average TOC based on all wells in the main area of interest where geochemical data is available (only wells included in the main database are marked). The map is generated with a convergent interpolation algorithm, and provides a general impression of the organic content variations. A comparison between average TOC from samples and average TOC predicted from equation 1 is shown in Table 2, indicating coherent ranges between the discrete and continuous TOC values. We obtain an average TOC of 5.5 and 5.1 wt. % for the Tau Formation, and 6.5 and 6.2 wt. % for the Draupne Formation (average values represent measurements and prediction from logs, respectively).

T_{max} values (Figure 5a) indicate that the maturity of organic-rich shales in the area range from mainly immature and early mature to oil window maturity, and most of the samples display $T_{max} < 435°C$. At the early mature stage, generation of fluid hydrocarbon has initiated, but substantial amounts and migration of hydrocarbons is most likely not present (Vernik and Landis, 1996). Hydrogen Index (HI) values range from 26–635 mg HC/g TOC.

The organic matter appears to vary between type II and type III, showing a slight zonation related to location (Egersund Basin, southwest and northeast Ling Depression, respectively). This is likely also influenced by differences in maturity (Dembicki, 2009), as HI values decrease with increasing T_{max}. Well completion reports and vitrinite reflectance values (R_o = 0.4–0.62%) typically indicate maturities between immature and early mature (Table 2). The exception is the reference well for geochemical data in the mature source rock area, 15/3-1S, which displays clear signs of peak oil window maturity considering HI–T_{max} values (Figure 5) and vitrinite reflectance (R_o = 0.6–0.88%). Data from wells 17/6-1, 17/3-1 and 15/3-1S are also displayed in a TOC–HI plot in Figure 5b. In addition to the Tau Formation, data from the younger Sauda Formation (17/6-1) and older Egersund Formation (17/3-1) are added for comparison. Vitrinite reflectance values at corresponding depths are also indicated.

Variation in acoustic impedance and the link to rock properties

AI and TOC have been shown to have a nonlinear relationship which can be used to quantify TOC from seismic data with a certain level of confidence (Løseth et al., 2011). A 1D conversion such as this has the requirement of obtaining a good relation between AI and TOC in nearby wells to validate and fit the general relationship, and good seismic to well correlation with respect to inverted impedance. As impedance responds to compaction (both mechanical and chemical), a relatively constrained depth range should be assessed to expect consistent results. This is shown in Figure 6a where AI for the Tau and Draupne Formations (all wells in database; Table 1) is plotted against depth (corrected for exhumation) and color coded with TOC. AI–TOC pairings can be seen to rapidly vary with minor depth variations. An additional consideration for our study area is that the source rock maximum burial depth fluctuates around the onset of hydrocarbon generation (from immature to oil mature), which

Interpretation 15

will similarly have an influence on the relation between AI, depth and TOC. Even though these complexities pose a challenge for accurately determining TOC, it can provide some insight into effects related to maturation. Significant maturation will potentially have a counteracting influence on typical compaction trends (decreasing porosity and stiffening) due to kerogen conversion to porosity and oil, i.e., hydrocarbon softening, and associated overpressure due to low permeability (Yenugu and Han, 2013). Considering a constrained TOC range of 5–7 wt. %, comparatively low AI is observed in more mature intervals below ~3 km or ~90°C (average geothermal gradient in the study area is 31.7°C/km). This behavior deviates from an almost linear compaction trend in data at shallower depths (Figure 6b). The need for a depth/maturity dependent AI–TOC relation is further exemplified in Figure 6c, where the development of increasing AI at low TOC content relative to depth seems to fairly coincide with trends suggested by Løseth et al. (2011). Note however that while the behavior of rocks buried deeper than ~3.3 km is similar (dark orange-brown), the highest AI at a given TOC corresponds to rocks at 2.9–3.3 km (lighter orange).

Similar features can be interpreted from the seismic data. Figure 7a and 7b shows the time-horizon for top Tau Formation in the northeast Ling Depression and relative AI extracted from 5 ms below the Tau horizon, respectively. The latter indicates impedance contrast between the Tau Formation and the overlying shale-dominated Sauda Formation. We can see an increasingly negative response (progressively larger contrast to the layer above) towards the deeper part of the basin, if comparing to the corresponding time map. Similarly, resulting absolute AI from the model-based inversion is displayed in Figure 7c on an arbitrary line from the location of well 17/6-1 in the east to the deeper basin area towards west (A to A'). Distinctly low AI is indicated for the Tau Formation across the line, yet it is most pronounced in the deeper section. We can also pick out high-contrast coal events in the Bryne

For Peer Review

Formation interval. At this stage, it would have been possible to apply empirical TOC transforms to predict organic content. As discussed above however, we would likely have introduced significant bias by not honoring burial depth, compaction, and where applicable, maturation effects.

~~If w~~We can exemplify this by considering the well log (depth) domain, ~~we can assign linear approximate maximum and minimum values in the AI depth~~ by first plotting~~ on~~ data from shales with great spread in TOC (Flekkefjord, Sauda, Tau, Draupne and Heather Formations) as AI versus depth. From there, data representing TOC ≈ 0 wt. % and maximum observed TOC can be described by linear trends. Any point at a given depth between these lines is represented by a value $0 < (AI_0 – AI_{log})/(AI_0 – AI_{max}) < 1$, if the AI values of these lines (AI_0 and AI_{max}, respectively) are expressed as functions of depth (i.e., $AI = a \times Z_{BSF} + b$). ~~we~~This value can be converted to TOC units by multiplying with the maximum TOC value observed in the calibration data. In our case, this formula is reduced to~~derive an empirical relation which incorporates both parameters to predict TOC, expressed as~~

$$\text{TOC (wt. \%)} = 0.0105\,(Z_{BSF} + 275 – 0.36\text{AI}). \quad (3)$$

Coefficients in equation 3 indicate the compaction trend (slope = –0.36), and range (difference in intercept = 275) of AI as a function of depth, referenced to maximum and minimum values. ~~A~~The scaling factor (0.0105) converts input values to the span of TOC. By including a depth term (Z_{BSF} = depth in meters below sea floor, corrected for exhumation if applicable), we obtain an empirical, more universal TOC–AI relationship~~predictions~~ in wells with different source rock maximum burial (Figure 8a). Note that this is not because depth and TOC are related, but because the effect of compaction on AI values is accounted for. Wells in Figure 8a have largely similar AI signature, but drastically variable organic content. Heather Formation in well 15/12-3 is included for validating lower TOC in deeper sections.

For Peer Review

We also indicate measured TOC values from samples (minimum – average – maximum) for each formation. Qualitative validation in two wells is shown in Figures 8b and 8c, where we in the latter can see that organic content is also identified in Bryne Formation coals, but poorly quantified. The proposed relation is limited to application in shales in the chemical compaction domain (i.e., not softer mudrocks that have only been compacted mechanically) and prior to the onset of hydrocarbon generation, i.e., a general effective range of 2–3 km depth BSF. Additionally, it would require a time–depth conversion to be applied to seismic. If some type of calibration data is available, the relation should be possible to utilize in other basins as there are no direct restrictions on ~~e.g.,~~ factors such as lithology.

Problems related to the non-uniqueness of rock property inversion for organic rich shales are also highlighted in Bandyopadhyay et al. (2012), who show how incorporating V_p/V_s in addition to AI reduces error (ambiguity due to combinations of clay volume, TOC and porosity) and produces better constrained results. Therefore, we investigate if incorporating additional seismic properties will result in equivalent or better TOC prediction, and potential for evaluating maturity and hydrocarbon presence.

Compaction trend and rock physics template

Non-source shale dominated formations defining our background shale trend (solid black line) are plotted in terms of V_p/V_s versus AI in Figure 9a (all data) and 9b (upscaled data). The brine saturated and gas saturated sand models are added to the template in Figure 9c, superimposed on sandstone data used for calibration. Data from the Tau and Draupne formations in all seven wells are shown as grey points. Our background shale compaction trend obtained locally is seen to closely resemble the published inorganic shale trend (Khadeeva and Vernik, 2014; Avseth and Carcione, 2015).

For Peer Review

We can see that overlap occurs mainly at greater depth (lower V_p/V_s and higher AI), where the properties of mature organic rich shale (lowermost cluster of grey points) coincide with both brine and hydrocarbon sandstones in well 15/3-8 (green and dark red points) at similar depth (Figure 9c). Sandstones from shallower sections have significantly lower V_p/V_s and higher AI than the depth-adjacent immature to early mature organic rich shale.

TOC effect in shales at intermediate maximum burial depth (2–3 km)

The constructed rock physics template for sandstone and non-organic shale is superimposed on available data from the organic-rich shale formations in Figure 10. Estimated maximum burial depth for the Tau and Draupne Formations in the available wells from the main area of interest is ~2–3 km (Table 1), whereas in well 15/3-8 top Draupne is encountered at 3.8 km. Initially omitting well 15/3-8, the values range from 5300 to 8000 g/cm^3 × m/s for AI and 1.85 to 2.3 for V_p/V_s.

Irrespective of lithostratigraphic nomenclature and lateral distances, the organic shale intervals with the shallowest maximum burial display a similar range of elastic properties. This is apparent when examining the Tau and Draupne Formations encountered in wells 17/12-4, 16/8-3S and 15/12-22 (top at ~2400–2600 m maximum burial; Figure 10a and 10b). Acoustic impedance varies between 5300–6200 g/cm^3 × m/s and the velocity ratio is within the range of 2.0–2.3 for these three wells. TOC is predicted to be partly lower in 17/12-4 (Tau Formation in the Egersund Basin; Figure 10c). The Draupne Formation of well 15/12-22 has the most constrained behavior, which is reflected also in uniform gamma and resistivity log responses throughout the formation, and TOC around 4–8 wt. % (Figure 10d). Well 9/2-11 (Tau Formation, Egersund Basin) is shifted in the direction of increasing compaction if compared to well 17/12-4, i.e., towards overall higher AI and lower V_p/V_s, as expected due to

For Peer Review

higher maximum burial depth (Figure 10a, Table 1). The organic content is similar in these well locations (Figure 10c). A similar shift can be observed in data from well 17/6-1 (Tau Formation, northeast Ling Depression; Figure 10a), which has a slightly shallower maximum burial depth compared to 9/2-11 (top Tau at ~2750 versus ~2860 m BSF), but a higher TOC content. Although there is overlap between these clusters, impedance and V_p/V_s values are (on average) lower in well 17/6-1, and appears roughly related to increasing TOC (Figure 10c).

The Draupne Formation in well 15/12-23 has similar properties to the shallow Draupne and Tau Formations in its upper section, whereas AI increases and V_p/V_s decreases towards the base (Figure 10b). TOC variation is limited and around 7 wt. % (Figure 10d). An upwards increasing gamma ray response is observed in this well, even though the uranium content is similar in the upper and lower parts of the formation. Minimum gamma ray readings are still relatively high (around 120 API). Deep resistivity measurements in all aforementioned wells are generally lower than ~4 ohm-m, except for the high-TOC part of the Tau Formation in well 17/6-1 where elevated values are recorded (Figures 10e and 10f).

Due to distances between the wells being studied, additional factors such as compositional and depositional differences can influence the elastic signatures and potentially obscure the independent effect of TOC. Kerogen substitution is applied to the Tau Formation shale in well 17/12-4, to predict elastic properties at different TOC levels (Vernik, 2016). We assume kerogen density ρ_k = 1.13 g/cm^3 based on $R_o \approx 0.5\%$ (Equation 2). By accepting the limitations and assumptions for the kerogen substitution, we can observe that Tau Formation data (TOC > 4 wt. %) is shifted onto the background shale trend when TOC is reduced to ~1 wt. % (Figure 11a). Varying TOC content gives a greater relative change in AI and a more subtle change in V_p/V_s than when comparing data from two different wells (e.g., 17/6-1 and 9/2-11 in Figure 10). Relations between deeper and shallower organic lean shales (Fjerritslev and Flekkefjord Formations), brine sandstone (Bryne Formation), and the in-situ and kerogen-substituted Tau Formation at the well location are shown as reference.

By shifting the compaction trend incrementally along the observed direction of increasing TOC in Figure 11a, we create trendlines that have an acceptable coherence with TOC variation in other wells. Due to high degree of scatter and overlap in data, quantification accuracy is not on the order of 1%, but we can delineate intervals such as <4, 4–8, and >8 wt. % (Figure 11b).

For Peer Review

Comparison to deeply buried, oil-mature source rock

Well 15/3-8 drilled in the Viking Graben to the northwest of the main study area, where the Draupne Formation is penetrated at much greater depth, has been included as a representative of deeply buried and mature source rock (Isaksen and Ledje, 2001). At the well location, the Draupne Formation is encountered at 3800 m BSF and is 659 m thick (including ~275 m intra-Draupne sands). As sand-shale variations occur in the Draupne Formation in this well, the properties of two intervals clearly dominated by shale, one in the upper and one in the lower part of the formation, have been extracted for analysis (3873–3930 m and 4262–4340 m BSF, respectively). The mature organic shale intervals in well 15/3-8 plot around the brine sandstone trend, display V_p/V_s around 1.8, lower than observed in shallower locations, and AI between 6500–9000 g/cm^3 × m/s (Figure 10b).

TOC for the Draupne shale in this area is around 2–8 wt. % based on the geochemical data from well 15/3-1S and predicted TOC in well 15/3-8. If attempting to characterize the mature source rock by comparing TOC content within the trends defined above for AI and V_p/V_s, there is a clear discrepancy compared to shallower source rock intervals (Figure 12).

These discrepancies indicate that additional processes have come into play at this depth, and resistivity indicates a presence of hydrocarbons (Figure 10f).

As described above in “Database and methods”, neither Gassmann fluid substitution nor the extrapolated mineralogy perfectly represents the Draupne shale in question. The predicted properties after substituting brine for oil shown in Figure 12, in accord with Lucier et al. (2011), are however noticeably more coherent with the TOC-segregated compaction trends described earlier. Fluid substitution results in a minor increase in impedance (~300 g/cm^3 × m/s) and higher V_p/V_s ratio (~0.15).

Bedding-normal velocity ratio and computed acoustic impedance based on the dataset adapted from Sondergeld et al. (2000) is shown in Figure 13a, color coded with TOC. They state that measurements were done soon after recovery and that care was taken to preserve the original fluids in place. Any effects of hydrocarbons on velocities and density of the shale should consequently be represented in these data. The measurements predominantly show AI between 7000 and 10000 g/cm^3 × m/s and V_p/V_s around 1.6–1.95, resembling data from well 15/3-8. P-wave anisotropy expressed by the Thomsen (1986) epsilon parameter is used as color code in Figure 13b for reference, indicating significant anisotropic behavior (ε = 0.1–0.35).

Considering alternative seismic attributes, source rock shale data is displayed in terms of λ–μ–ρ, colored firstly according to well in Figure 14a. TOC displays a negative correlation to $\lambda\rho$ which is in the range of 15–35 GPa × g/cm^3, and we observe a restricted $\mu\rho$ range from 6 to 14 GPa × g/cm^3 in immature to early-mature source rocks (Figure 14b). Increasing $\mu\rho$ is associated with increasing depth of occurrence and consequent rock stiffness (degree of cementation) as described above.

Whereas $\lambda\rho$ is similar for all wells, the $\mu\rho$ attribute increases further as a function of depth and ranges from around 13–24 GPa × g/cm^3 in the mature Draupne shale (Figure 14a). We can again observe the relatively larger discrepancy in well 15/3-8 compared to the background trend, particularly where resistivity is high (Figure 14c), than shallower organic-rich shale intervals.

Synthetic AVO classification

AVO responses corresponding to top source rock in each of the seven wells (containing V_s measurements) are presented in Figure 15. Averaging block size of 3 m or 10 m is seen to have minor impact on the absolute intercept and gradient values. The primary interpretation of these data is that all wells have a predicted in-situ AVO class IV signature, with the exception of a weak class III response in well 17/12-4. No apparent pattern can be pinpointed with respect to increasing burial depth. For the Tau Formation, the gradient slightly increases with increasing burial, whereas the opposite can be seen for the Draupne Formation. The Draupne Formation display somewhat higher intercept values, except for well 16/8-3S where the top source rock reflector is barely distinguished from the background trend.

DISCUSSION

Changes in elastic properties as a function of increasing burial and compaction can easily be observed in our data (e.g., Figures 6 and 9), and subsequently accounted for when assessing the TOC and hydrocarbon trends. This type of compaction behavior for organic-rich and organic-lean shale is previously established and discussed in various papers (e.g., Dræge et al., 2006; Løseth et al., 2011; Avseth and Carcione, 2015). We can also observe the

For Peer Review

potential for ambiguity between shaly sands (closer to shale trend) and well-compacted shales, as well as poorly consolidated sands and organic-rich shales (Figure 9).

Effect of TOC

The maximum burial depth and geochemical parameters in several analyzed wells indicate temperatures too low to invoke substantial generation of hydrocarbons. Consequently, they may provide a good reference for interpretation of effects related to variations in organic matter and compaction. Based on well log data from our study area, shale intervals that have relatively good source rock potential but organic content less than ~3–4 wt. % display similar elastic properties as shales with negligible organic content and source rock potential (Figures 9 and 10). This is important when assessing a larger area where depth variations may be significant for a given formation.

We infer the potential ambiguity in for instance applying direct transforms between AI and TOC on a seismic section (Figures 6 and 7) without knowing the contribution of compaction and fluid softening on the impedance values. The proposed empirical relation for TOC prediction (equation 3) partially addresses the issue by incorporating depth, whereas the influence of maturity and hydrocarbon generation is more complex to quantify via a single elastic parameter. For TOC > 3 wt. %, we deem it reasonable that TOC can be related linearly to AI at a given depth. For lower amounts of organic content, our relation will likely provide a slight underestimation (Figure 8a), as AI has been shown to increase more rapidly with decreasing TOC in the lower segment (Løseth et al., 2011).

If only considering a very restricted depth interval, source rock formations will typically have significantly lower acoustic impedance, even at lower levels of organic content (Løseth et al., 2011). Our results also suggest slightly lower V_p/V_s ratio than in non-source

For Peer Review

shales (Figures 10, 11a and 11b). Overall decreasing V_p/V_s and AI with increasing TOC agree with previous findings (Løseth et al., 2011; Vernik and Milovac, 2011; Guo et al., 2013; Sun et al., 2013; Zhao et al., 2016; Vernik et al., 2018). Laboratory measurements indicate a similar and clear TOC trend in the V_p/V_s–AI space compared to the well log data (Figure 13a). Using rock physics modeling, Zhao et al. (2016) show how maturation and the amount of quartz and feldspar influence the response in V_p/V_s to changing TOC. Our observed reduction in V_p/V_s from increasing organic content is not necessarily universal for other shales and basins, and is likely observed due to the clay-rich nature of the Tau and Draupne Formations. Sun et al. (2013) similarly show how clay content can alter the TOC effect.

The observed effect of TOC is supported by kerogen substitution modeling, predicting a dominant change in AI and a minor change in V_p/V_s. Dark grey shales of the Flekkefjord and Fjerritslev Formations display properties consistent with the modeled ~1 wt. % TOC Tau Formation in terms of compaction. TOC in the study area is on average 1.3 ± 0.9 wt. % for the Flekkefjord Formation and 1.3 ± 0.5 wt. % in the Fjerritslev shales (NPD, 2017). They are consequently assumed to be overall similar to the Tau Formation on a kerogen-free basis. The shift observed in Figure 11a is therefore seen as a reasonable approximation of the direct effect kerogen had on this particular shale.

Subsequently, our compaction-consistent TOC increments are used to relieve the consideration of depth. We see that immature to early mature shales with similar TOC compact along the same trend, but at lower absolute AI and V_p/V_s compared to organic-lean counterparts (Figure 11b). The trends only appear valid down to a certain depth where advanced maturation processes initiate (Figure 12), which are discussed in the subsection "Effect of maturation and hydrocarbon generation" below.

For Peer Review

Additionally, we demonstrate how decreasing $\lambda\rho$ provide fairly good discrimination of TOC in immature to early mature intervals (Figure 14b), whereas $\mu\rho$ is naturally a good indicator of increasing compaction and associated shear stiffness which can be a result of cementation. Mineralogical differences also influence the strength and stiffness of the rock composite. Extensive data on the composition of the Draupne and Tau Formations in literature are rare, but published results are considered where possible (Kalani et al., 2015b; Zadeh et al., 2017). Changes in depositional settings and seafloor conditions at the time of deposition could vary over relatively short distances laterally and temporally, but these studies show from XRD that the organic-rich shales are dominated by clay in the study area (40–80%). Most abundant are kaolinite (30–65% of total clay), smectite, illite and mixed-layer I/S (in sum 25–65% of total clay). Quartz constitutes 10–24% of the bulk mineralogy (Kalani et al., 2015b; Zadeh et al., 2017). For well 15/3-8 in the Viking Graben, apparent silty and sandy intervals have been excluded based on log signatures.

Effect of maturation and hydrocarbon generation

The principal changes in elastic properties expected to coincide with maturation of organic-rich shales are the effects of increasing compaction and diagenesis (Figures 6 and 10). Secondly, TOC has been shown both in previous studies and in data herein to have a significant effect on velocity and density (e.g., Vernik and Landis, 1996). This effect moves data in a different direction in the V_p/V_s–AI space compared to the compaction trend (Figures 10 and 11). Consequently, only by simultaneously taking these two dominating factors into consideration, the effects of oil (and gas) generation in source rocks can be evaluated. Our results also suggest that even though TOC can be evaluated in terms of a single seismic

For Peer Review

attribute, in our case AI (Figures 6 and 8), incorporation of shear wave information grants better insight into the interplay between compaction, TOC and maturity (Figure 12).

Considering the wells containing V_s, six out of seven penetrate source rock shales within a relatively narrow range of maturity from immature to early oil window. This maturity range is indicated by geochemical data from representative wells, namely T_{max} versus HI and vitrinite reflectance (Figure 5a), ΔlogR signatures, and the range of maximum burial (2.4–2.9 km BSF) with typically associated temperatures.

Practically indistinguishable source rock elastic properties in wells 17/12-4, 15/12-22, and 16/8-3S are explained by geological similarities in terms of structural setting, maximum burial depth, TOC, and indicated immaturity (Figure 10). These three are the shallowest of the six aforementioned wells, display low resistivity, and do not suggest any influence of thermal maturation. On the other hand, organic-rich shales found in wells 17/6-1, 15/12-23, and 9/2-11 are predicted to have the highest maximum burial of the six, which is reflected in their elastic properties with respect to the compaction trend (Table 1; Figure 10).

Firstly, no hydrocarbon generation is indicated in well 9/2-11. It is drilled on the flank of the Egersund Basin (Figure 1), and records low resistivity (<2–3 ohm-m) in the Tau Formation. Oil in the nearby Yme Field is explained by a mature source pod in the deepest part of the basin, based on chemical and isotopic oil composition and corresponding predicted maturity (Ritter, 1988; NPD, 2017). Only well 9/2-2 closer to the basin center indicates approaching oil window maturity for the Tau Formation, which is 600 m deeper than in well 9/2-11 (Table 2).

Similarly, we observe slightly increasing burial towards the west in the southwest Ling Depression, i.e., from well 15/12-22, via 15/12-23 to 15/12-3 (Figure 16; see Figures 1 and 4a for location). A more pronounced ΔlogR (qualitative maturity indicator) and resistivity up to

For Peer Review

20 ohm-m in the lower part of the Draupne Formation in well 15/12-3 could point towards initial hydrocarbon generation. However, T_{max}, HI and vitrinite reflectance all point towards immaturity or, at maximum, earliest mature considering the currently used reference values (Table 2 and Figure 5a). Top Draupne Formation in this well is 2886 m BSF, only 33 m deeper than in 15/12-23 where there is no elevated resistivity (Figures 10b and 16). A substantial difference in degree of maturation over such a small depth interval is not expected, but simultaneously, the considered wells are within a constrained area, which should serve to minimize differences in provenance and depositional environment.

Comparable elevated resistivity is observed in well 17/6-1 in the Ling Depression, up to ~15 ohm-m. Geochemical data are to some extent ambiguous, but generally points towards immature to early mature source rock. A vitrinite reflectance value of 0.43 ± 0.06 % is recorded at 2507 mRKB (2767 m BSF after correcting for approximate exhumation), slightly above the middle of the formation. T_{max} values <435°C also contradict hydrocarbon generation (Figure 5a). The lower part of the Tau Formation has relatively low HI compared to its high TOC (Figure 5b), which can be interpreted as a sign of increasing maturity (compared to vitrinite reflection equivalents from Vernik and Landis, 1996), but no R_o readings are available for validation. On the other hand, the vitrinite reflectance value reported for well 17/3-1 in the same area is substantially higher, and TOC–HI values are consistent with the R_o reference lines (Figure 5b). Oil window maturity is consequently indicated for the Tau Formation in well 17/3-1, which is in conflict with low resistivity (<6 ohm-m) and ~200 m shallower burial depth than in well 17/6-1.

Unlike the SW Ling Depression (15/12-3), the eastern part of the study area has been subjected to exhumation, in response to Oligocene and Miocene uplift of southern Norway and glacial erosion in the Pliocene and Pleistocene (Jordt et al., 1995). As maturation of

For Peer Review

organic matter and hydrocarbon generation is a function of the time–temperature integral (Connan, 1974), uplift could intervene with oil generation depending on timing. Based on kinetic models of the deeper parts of the neighboring Egersund Basin, Ritter (1988) suggest an approximate Eocene onset of oil generation, i.e., preceding upliftment by a few million years. The minor, inconsistent signs of initial maturation for the NE Ling Depression are thus assumedly inherited from maximum burial (pre-uplift), and separation between wells 17/6-1 and 9/2-11 in the V_p/V_s–AI crossplot is predominantly explained by different TOC content.

In sum, our observations so far may hint that wells encountering organic rich shales close to a depth of 2.9 km (BSF) in our area are barely missing the threshold for onset of oil generation. An average geothermal gradient of 31.7°C/km in the study area is consistent with this depth, assuming that oil generation initiates around 90°C (Bjørlykke, 2015). Therefore, deeper Ling Depression areas for instance could contain more mature source rock than recorded in wells, analogous to the Egersund Basin. Poststack inversion results indicate further softening of the Tau Formation towards deeper parts of the basin compared to the 17/6-1 well location (Figure 7). With prestack seismic data, closer examination of TOC–maturity relations in that area would be possible with the aid of interpretations in the V_p/V_s–AI domain.

Our database consequently only contains one well with measured V_s penetrating unambiguously mature source rock where hydrocarbons are generated (15/3-8, peak to late oil window). Comparatively different elastic and petrophysical properties observed in the upper and lower Draupne shale can be explained by low TOC and associated lower hydrocarbon generation potential in the latter. An increase in AI corresponds to increasing depth and decreasing TOC within the formation (Figure 10). Additionally, high resistivity indicating hydrocarbon saturation (Passey et al., 1990) is clearly pronounced in the upper

For Peer Review

Draupne shale (deep resistivity up to 100 ohm-m), whereas resistivity values in the lower part with less organic content are lower and similar to well 17/6-1 (<15 ohm-m).

From a petrophysical perspective, elevated resistivity is normally related to the presence of hydrocarbons in open/connected pore space (e.g., in sandstone reservoirs). However, the permeability of mudrocks is usually extremely low (vertically as low as 10^{-1}–10^{-5} mD; Mondol, 2009; Mathur et al., 2016) without the aid of additional processes such as microfracturing. Microfracturing in source rocks is associated with hydrocarbon-generated overpressure (e.g., Vernik, 1994; Vernik and Landis, 1996; Kalani et al., 2015b; Zadeh et al., 2017), and resistivity anomalies could therefore potentially indicate amounts of oil generation sufficient to initiate intra-shale migration and potentially expulsion. . Resistivity tools also respond to different minerals, meaning that a direct correlation between minor resistivity increases (e.g., well 17/6-1) and the presence of hydrocarbons is prone to uncertainty.

Interestingly, we observe how fluid substitution indicates that hydrocarbon saturation owing to a higher maturity rank reasonably explains the discordance between our TOC–compaction trends and the Draupne Formation elastic properties in well 15/3-8. This feature is incorporated in Figure 17, which summarizes our findings with a schematic interpretation of the V_p/V_s–AI data in relation to the rock physics template. Data are represented by average V_p/V_s, AI and TOC of each well penetrating the source rock interval. The averages provide exaggerated separation for clarity, whereas in the log scale data (Figure 11b) a higher degree of overlap is observed. We also note that data recorded with ~1 km depth difference (15/3-8 and 17/6-1) display only moderate divergence in the direction of compaction (~porosity) compared to differences observed in the shallower intervals. Compaction-related porosity loss could potentially have been overprinted in the elastic properties by porosity created from conversion of kerogen to oil (organic pores; Alfred and Vernik, 2012).

For Peer Review

Interpretation 30

Quantitative changes in elastic properties as a result of maturation, initial migration and expulsion of hydrocarbons can consequently be suspected to be subtle (but noticeable) when considering for instance the resolution of seismic inversion data. The clearest indications of hydrocarbon generation are likely observed after excluding the effect of compaction and understanding the local TOC-variation (Figure 17). The latter can be achieved by employing a method such as suggested by Løseth et al. (2011) where a TOC profile can be derived from inverted P-impedance alone, or by calibrating TOC interval trends to well data in the V_p/V_s–AI space as shown in this study. Both exhumation and the inherent episodic nature of oil migration/expulsion are also most likely important factors to consider in relation to overpressure and microfracturing (e.g., opening and closing of fractures).

We do not find λ–μ–ρ analysis to have any obvious advantage over V_p/V_s–AI in terms of characterizing immature and mature source rocks simultaneously, as both attribute domains depend on a representative background shale trend. Increasing compaction relates linearly to increasing $\mu\rho$, but both increasing TOC and increasing maturity are represented by increasingly low $\lambda\rho$ values compared to the compaction trend (Figure 14). Using a constant $\lambda\rho$ value as a fluid indicator like in sandstones (e.g., 20 GPa × g/cm^3; Goodway et al., 1997) would not serve to separate immature from mature source rocks.

Another commonly discussed issue is upscaling errors, related to comparing laboratory measurements, well logs and seismic data all at different resolutions. Comparisons to ultrasonic data in our study increases our confidence that at least well log data (averaged and raw) capture the geologic variations observed on the laboratory scale with reasonable accuracy. Simultaneously, significant anisotropy indicates that there could be challenges related to comparing predicted and real seismic properties (Sondergeld et al., 2000). Bedding-

For Peer Review

normal ultrasonic core measurements and sonic log data have also been shown by Vernik and Milovac (2011) to be similar for organic-rich shales.

AVO implications

The prediction of AVO class IV behavior is recurring for all top source rock interfaces (except a weak class III response in well 17/12-4) regardless if the organic shale in some areas has significantly shallower maximum burial (Figure 15). It is interesting to note that the mature source rock in well 15/3-8 which is influenced by liquid hydrocarbon, also shows AVO class IV behavior based on the synthetic AVO modeling. Consequently, AVO class alone does not appear to discriminate the degree of maturation. Intercept value, i.e., zero offset reflection coefficient, is noticeably higher in well 15/3-8 compared to some of the other wells, consistent with findings in Carcione and Avseth (2015) which indicate that increasing gas saturation/maturity results in higher values of $R_{pp}(0)$. However, wells 15/12-22 and 15/12-23 also have high intercept values. Comparison to the individual background trends, however, show that the anomaly observed for top Draupne Formation in well 15/3-8 is greater than for other locations. Quantification of deviations from the background shale trend, similar to the fluid factor theory, can potentially be applied on real prestack AVO data for more detailed interpretations of fluid sensitivity and signs of oil generation and expulsion (Smith and Gidlow, 1987; Castagna et al., 1998).

CONCLUSIONS

Links between compaction, organic content, maturation and seismic properties were postulated through rock physics crossplots. A summary of key observations from this study follows:

For Peer Review

1) Local compaction trends in elastic properties can be excluded based on organic-lean shale data (represented by decreasing V_p/V_s and increasing AI). Average TOC in the Tau and Draupne Formations span from ~2.3 to 9.6 wt. % in our study. Increasing TOC has been shown previously and in our data to reduce both V_p/V_s and acoustic impedance in clay-rich shales, meaning that it works obliquely to the effect of increasing burial and compaction. Compaction trends shifted according to the behavior predicted by kerogen substitution capture incremental TOC variations successfully, but are only valid for shales encountered shallower than ~3 km (BSF) and corresponding maturation stages. Where only acoustic impedance is available, we suggest a relation which incorporates AI and burial depth to predict TOC.
2) A mature source rock, given its TOC content, represents a palpable deviation from TOC–compaction trends valid for immature organic-rich shales. A fluid effect, indicated by high resistivity and predicted by fluid substitution, reasonably explains this discordance. We therefore infer a potential for extracting information about both organic richness and hydrocarbon generation from seismic data.
3) Comparison to ultrasonic measurements of the Kimmeridge shale indicates that upscaling is not distorting our interpretations. Understanding how the significant anisotropy will affect inversion of real seismic data will however require further consideration.

ACKNOWLEDGEMENTS

Firstly, we are sincerely thankful for the support and funding provided by Eni Norge for the ReSource project ("Quantitative Analysis of **Re**servoir, Cap and **Source** Rocks of the Central North Sea"). We would like to thank Kristoffer Løvstad, Henrik N. Hansen and Jens Jahren at the University of Oslo and Filippos Tsikalas at Eni Norge for helpful discussions

For Peer Review

and input. All data are provided through the courtesy of DISKOS and NPD. Academic software licenses have been provided by Lloyd's Register for Interactive Petrophysics, Ikon Science for RokDoc, CGG for Hampson-Russell, and Schlumberger for Petrel.

REFERENCES

Aki, K. and P. G. Richards, 1980, Quantitative Seismology: Freeman.

Alfred, D. and L. Vernik, 2012, A new petrophysical model for organic shales.: SPWLA 53rd Annual Logging Symposium.

Avseth, P. and J. M. Carcione 2015, Rock-physics analysis of clay-rich source rocks on the Norwegian Shelf: The Leading Edge, **34**, 936-943.

Badics, B., A. Avu and S. Mackie 2015, Assessing source rock distribution in Heather and Draupne Formations of the Norwegian North Sea: A workflow using organic geochemical, petrophysical, and seismic character: Interpretation, **3**, 45-68.

Bandyopadhyay, K., R. Sain, E. Liu, C. Harris, A. Martinez and M. Payne, 2012, Rock property inversion in organic-rich shale: Uncertainties, ambiguities, and pitfalls: 82nd Annual International Meeting, SEG, 1-5.

Bjørlykke, K. 1998, Clay mineral diagenesis in sedimentary basins — a key to the prediction of rock properties. Examples from the North Sea Basin: Clay Minerals, **33**, 15-34.

Bjørlykke, K., 2015, Petroleum Geoscience. From Sedimentary Environments to Rock Physics - Second Edition: Springer-Verlag Berlin Heidelberg.

Carcione, J. M. 2000, A model for seismic velocity and attenuation in petroleum source rocks: GEOPHYSICS, **65**, 1080-1092.

Carcione, J. M. and P. Avseth 2015, Rock-physics templates for clay-rich source rocks: GEOPHYSICS, **80**, no. 5, D481-D500.

Castagna, J. P. and H. W. Swan 1997, Principles of AVO crossplotting: The Leading Edge, **16**, 337-342.

Castagna, J. P., H. W. Swan and D. J. Foster 1998, Framework for AVO gradient and intercept interpretation: GEOPHYSICS, **63**, 948-956.

Connan, J. 1974, Time-temperature relation in oil genesis: AAPG Bulletin, **58**, 2516-2521.

Dang, S. T., C. H. Sondergeld and C. S. Rai 2016, A New Approach to Measuring Organic Density: Petrophysics, **57**, 2, 112-120.

Dembicki, H. 2009, Three common source rock evaluation errors made by geologists during prospect or play appraisals: AAPG Bulletin, **93**, 341-356.

Dræge, A., M. Jakobsen and T. A. Johansen 2006, Rock physics modelling of shale diagenesis: Petroleum Geoscience, **12**, 49-57.

Faleide, J. I., F. Tsikalas, A. J. Breivik, R. Mjelde, O. Ritzmann, Ø. Engen, J. Wilson and O. Eldholm 2008, Structure and evolution of the continental margin off Norway and the Barents Sea: Episodes, **31**, 82-91.

Gautier, D. L. 2005, Kimmeridgian Shales Total Petroleum System of the North Sea Graben Province: U.S. Geological Survey Bulletin, **2204-C**, 1-24.

Goodway, B., T. Chen and J. Downton, 1997, Improved AVO fluid detection and lithology discrimination using Lamé petrophysical parameters; "λρ", "μρ", & "λ/μ fluid stack", from P and S inversions: 67th Annual International Meeting, SEG, Expanded Abstracts, 183-186.

Guo, Z., X.-Y. Li, C. Liu, X. Feng and Y. Shen 2013, A shale rock physics model for analysis of brittleness index, mineralogy and porosity in the Barnett Shale: Journal of Geophysics and Engineering, **10**, 1-10.

Hansen, J. A. and N. H. Mondol, 2018, Predicting the effects of organic content and maturation on the elastic properties of Central North Sea source rocks: 80th EAGE Conference and Exhibition 2018, Expanded Abstracts.

Hansen, J. A., H. D. Yenwongfai, M. Fawad and N. H. Mondol, 2017, Estimating exhumation using experimental compaction trends and rock physics relations, with continuation into analysis of source and reservoir rocks: Central North Sea, offshore Norway: 88th Annual International Meeting, Expanded Abstracts, 3971-3975.

Ibrahim, M. A. and T. Mukerji, 2017, Thermal maturation effects on the elastic properties of organic rich mudrocks: 87th Annual International Meeting, SEG, Expanded Abstracts, 3955-3960.

Isaksen, G. H. and K. H. I. Ledje 2001, Source rock quality and hydrocarbon migration pathways within the greater Utsira High area, Viking Graben, Norwegian North Sea: AAPG Bulletin, **85**, 861-883.

Japsen, P. 1998, Regional velocity-depth anomalies, North Sea chalk: A record of overpressure and neogene uplift and erosion: AAPG Bulletin, **82**, 2031-2074.

Jordt, H., J. I. Faleide, K. Bjørlykke and M. T. Ibrahim 1995, Cenozoic sequence stratigraphy of the central and northern North Sea Basin: tectonic development, sediment distribution and provenance areas: Marine and Petroleum Geology, **12**, 8, 845-879.

Kalani, M., J. Jahren, N. H. Mondol and J. I. Faleide 2015a, Compaction processes and rock properties in uplifted clay dominated units - the Egersund Basin, Norwegian North Sea: Marine and Petroleum Geology, **68**, 596-613.

Kalani, M., J. Jahren, N. H. Mondol and J. I. Faleide 2015b, Petrophysical implications of source rock microfracturing: Internation Journal of Coal Geology, **143**, 43-67.

Khadeeva, Y. and L. Vernik 2014, Rock-physics model for unconventional shales: The Leading Edge, **33**, 318-322.

Lash, G. and T. Engelder 2005, An analysis of horizontal microcracking during catagenesis: Example from the Catskill delta complex: AAPG Bulletin, **89**, 1433-1449.

Lucier, A. M., R. Hofmann and L. T. Bryndzia 2011, Evaluation of variable gas saturation on acoustic log data from the Haynesville Shale gas play, NW Louisiana, USA: The Leading Edge, **30**, 3, 300-311.

Løseth, H., L. Wensaas, M. Gading, K. Duffaut and M. Springer 2011, Can hydrocarbon source rocks be identified on seismic data?: Geology, **39**, 1167-1170.

Mannie, A. S., C. a.-L. Jackson and G. J. Hampson 2014, Structural controls on the stratigraphic architecture of net-transgressive shallow-marine strata in a salt-influenced rift basin:Middle-to-Upper Jurassic Egersund Basin,Norwegian North Sea: Basin Research, **26**, 675-700.

Mathur, A., C. H. Sondergeld and C. S. Rai, 2016, Comparison of steady-state and transient methods for measuring shale permeability: SPE Low Perm Symposium, SPE-180259-MS, 1-15.

Meyer, B. L. and M. H. Nederlof 1984, Identification of source rocks on wireline logs by density/resistivity and sonic transit time/resistivity crossplots: AAPG Bulletin, **68**, 121-129.

For Peer Review

Mondol, N. H., 2009, Porosity and permeability development in mechanically compacted silt-kaolinite mixtures: 79th Annual International Meeting, SEG, Expanded Abstracts, 2139-2143.
Mondol, N. H., K. Bjørlykke and J. Jahren 2008, Experimental compaction of clays: relationship between permeability and petrophysical properties in mudstones: Petroleum Geoscience, **14**, 319-337.
NPD. 2014, The 2014 Norwegian Petroleum Directorate lithostratigraphic charts, http://www.npd.no/en/Topics/Geology/Lithostratigraphy/, last updated 5. November 2014.
NPD. 2017, Norwegian Petroleum Directorate FactPages, http://factpages.npd.no/, accessed 15. September 2017.
Passey, Q. R., K. M. Bohacs, W. L. Esch, R. Klimentidis and S. Sinha, 2010, From oil-prone source rock to gas-producing shale reservoir – geologic and petrophysical characterization of unconventional shale-gas reservoirs: CPS/SPE International Oil & Gas Conference and Exhibition, SPE.
Passey, Q. R., S. Creaney, J. B. Kulla, F. J. Moretti and J. D. Stroud 1990, A practical model for organic richness from porosity and resistivity logs: AAPG Bulletin, **74**, 1777-1794.
Pedersen, J. H., D. A. Karlsen, K. Backer-Owe, J. E. Lie and H. Brunstad 2006, The geochemistry of two unusual oils from the Norwegian North Sea: implications for new source rock and play scenario: Petroleum Geoscience, **12**, 85-96.
Peltonen, C., Ø. Marcussen, K. Bjørlykke and J. Jahren 2009, Clay mineral diagenesis and quartz cementation in mudstones: The effects of smectite to illite reaction on rock properties: Marine and Petroleum Geology, **26**, 887-898.
Ritter, U. 1988, Modelling of hydrocarbon generation patterns in the Egersund Sub-Basin, North Sea: Advances in Organic Geochemistry, **13**, 1-3, 165-174.
Sayers, C. 2013a, The effect of kerogen on the AVO response of organic-rich shales: The Leading Edge, **32**, 1514-1519.
Sayers, C. 2013b, The effect of kerogen on the elastic anisotropy of organic-rich shales: GEOPHYSICS, **78**, no. 2, D65-D74.
Smith, G. C. and P. M. Gidlow 1987, Weighted stacking for rock property estimation and detection of gas: Geophysical Prospecting, **35**, 993-1014.
Sondergeld, C. H. and C. S. Rai 2011, Elastic anisotropy of shales: The Leading Edge, **30**, 324-331.
Sondergeld, C. H., C. S. Rai, R. W. Margesson and K. J. Whidden, 2000, Ultrasonic measurement of anisotropy on the Kimmeridge Shale: 70th Annual International Meeting, SEG, Expanded Abstracts, 1858-1861.
Sun, S. Z., Y. Sun, C. Sun, Z. Liu and N. Dong, 2013, Methods of calculating total organic carbon from well logs and its application on rock's properties analysis: GeoConvention 2013: Integration, AAPG/CSPG.
Thomsen, L. 1986, Weak elastic anisotropy: GEOPHYSICS, **51**, 1954-1966.
Thyberg, B. and J. Jahren 2011, Quartz cementation in mudstones: sheet-like quartz cement from clay mineral reactions during burial: Petroleum Geoscience, **17**, 55-63.
Vernik, L. 1994, Hydrocarbon-generation-induced microcracking of source rocks: GEOPHYSICS, **59**, 555-563.
Vernik, L., 2016, Seismic petrophysics in Quantitative Interpretation: Society of Exploration Geophysicists.

For Peer Review

Vernik, L., J. P. Castagna and S. J. Omovie 2018, S-wave velocity prediction in unconventional shale reservoirs: GEOPHYSICS, **83**, no. 1, MR35-MR45.
Vernik, L. and C. Landis 1996, Elastic anisotropy of source rocks-implications for hydrocarbon generation and primary migration: AAPG Bulletin, **80**, 531-544.
Vernik, L. and J. Milovac 2011, Rock physics of organic shales: The Leading Edge, **30**, 318-323.
Yenugu, M. and D.-H. Han, 2013, Seismic characterization of kerogen maturity: An example from Bakken shale: 83rd Annual International Meeting, SEG, Expanded Abstracts, 2773-2777.
Yenugu, M. and L. Vernik 2015, Constraining seismic rock-property logs in organic shale reservoirs: The Leading Edge, **34**, 1326-1331.
Zadeh, M. K., N. H. Mondol and J. Jahren 2016, Compaction and rock properties of Mesozoic and Cenozoic mudstones and shales, northern North Sea: Marine and Petroleum Geology, **76**, 344-361.
Zadeh, M. K., N. H. Mondol and J. Jahren 2017, Velocity anisotropy of Upper Jurassic organic-rich shales, Norwegian Continental Shelf: GEOPHYSICS, **82**, no. 2, C61-C75.
Zhao, L., X. Qin, D.-H. Han, J. Geng, Z. Yang and H. Cao 2016, Rock-physics modeling for the elastic properties of organic shale at different maturity stages: GEOPHYSICS, **81**, no. 5, D527-D541.
Zhao, L., X. Qin, J. Zhang, X. Liu, D.-H. Han, J. Geng and Y. Xiong 2018, An Effective Reservoir Parameter for Seismic Characterization of Organic Shale Reservoir: Surveys in Geophysics, **39**, 509-541.
Zhu, Y., S. Xu, M. Payne, A. Martinez, E. Liu, C. Harris and K. Bandyopadhyay, 2012, Improved rock-physics model for shale gas reservoirs: 82nd Annual International Meeting, SEG, Expanded Abstracts, 1-5.
Ziegler, P. A. 1992, North Sea rift system: Tectonophysics, **208**, 55-75.
Ødegaard, E. and P. Avseth 2004, Well log and seismic data analysis using rock physics templates: First Break, **23**, 37-43.

For Peer Review

LIST OF FIGURES

Figure 1: (a) Overview map showing location of the study area. (b) Detail view of the study area showing Central North Sea structural elements (NPD, 2017) and wells included in the database. Producing fields (presently or in the past) are marked with grey shading. The TA0701 3D seismic survey is outlined with a stippled rectangle.

Figure 2: Generalized Mesozoic stratigraphic succession in the study area (modified from NPD, 2014).

Figure 3: Comparison of TOC calculated from the ΔlogR method (Passey et al., 1990; dotted line) and from bulk density through equation 1 (solid line), with measured TOC (black dots)

For Peer Review

in calibration well 15/12-3. Gamma ray is shown to the left and resistivity-sonic overlay to the right. A crossplot of predicted versus measured TOC is shown below.

Figure 4: (a) Two way time (TWT) map of top Tau and Draupne formations from available 2D seismic data. (b) TOC distribution based on well data points (average per well). Note that the map is based on all locations with geochemical data in the area, but only wells included in our main database are shown for reference.

Figure 5: (a) T_{max} versus HI plot used as a kerogen type and thermal maturity indicator (Isaksen and Ledje, 2001). Green points are from southwest Ling Depression, red points from northeast Ling Depression and Åsta Graben, and black points are from the Egersund Basin (E.B.). Grey points are from the mature southern Viking Graben reference area (V.G.). (b) TOC versus HI for well 15/3-1S, 17/6-1 and 17/3-1 (Sauda and Egersund formations for comparison). Also indicated are associated vitrinite reflectance readings and reference lines from Vernik and Landis (1996).

Figure 6: (a) AI versus depth with TOC color code. Stippled grey lines are adapted from Løseth et al. (2011). (b) AI versus depth with resistivity color code (data with 5 < TOC < 7 wt. %. (c) Comparison between AI–TOC trends from Løseth et al. (2011) and data from the study area, color coded with depth.

Figure 7: (a) Map of top Tau Formation in TWT (s) based on 3D seismic data outlined in Figure 1, with location of arbitrary line A–A'. (b) Relative AI extracted 5 ms below the top Tau reflector showing relatively increasing contrast to the layer above towards deeper part of

For Peer Review

basin. Position of well 17/6-1 is indicated by the red point. (c) Inverted AI displayed along line A–A'. Top Tau, top Egersund and top Bryne horizons are shown for reference along with gamma ray log and formation tops in well 17/6-1.

Figure 8: (a) Realizations of equation 3, relating AI and depth (below sea floor, corrected for exhumation) to TOC, superimposed on data from organic-rich shale intervals in five wells. TOC predicted from equation 3 is shown in well 15/12-3 (b) and well 17/6-1 (c) compared to TOC from Rock-Eval (black points).

Figure 9: V_p/V_s–AI crossplot color coded with depth (km BSF) corrected for exhumation, showing background non-organic shales with (a) recorded well log scale and (b) ~3 m upscaling. The fitted black line corresponds with expected compaction behavior in this domain. Dotted lines indicate approximate range between maximum and minimum values. (c) Calibration of V_p/V_s–AI sandstone trends to data from the study area. Source rock shale data are shown as grey points, and the empirical background shale trend and a published inorganic shale trend are included for reference (Khadeeva and Vernik, 2014; Avseth and Carcione, 2015).

Figure 10: Organic rich shale formations (Tau and Draupne in left and right column, respectively) plotted on V_p/V_s–AI RPT calibrated to the study area, upscaled data. Color code represents well number (a, b), TOC (c, d) and deep resistivity (e, f).

Figure 11: (a) Comparison between the Tau Formation (well 17/12-4) in situ ($4 < TOC < 7$ wt. %) and after kerogen substitution in the V_p/V_s–AI plot, shown with shallower and deeper

For Peer Review

organic lean shales (Flekkefjord and Fjerritslev formations, respectively) and brine sandstone (Bryne Formation). (b) V_p/V_s–AI data from the source rock intervals in six wells within immature to early mature stages. Shifted compaction trends coarsely capture increasing TOC in data on the well log scale.

Figure 12: Upscaled data from seven wells superimposed on “constant-TOC” compaction lines, color coded with TOC. Replacing in-situ oil (green) with brine (blue) in the upper Draupne shale (well 15/3-8) is expressed with average V_p/V_s and AI before and after fluid substitution. Notice that the brine-scenario shows improved coherence with the TOC trendlines.

Figure 13: Ultrasonic measurements from Sondergeld et al. (2000) expressed in the V_p/V_s–AI crossplot with color code according to (a) TOC and (b) P-wave anisotropy expressed by epsilon (ε). Notice overall similar trend in TOC as described in well log data, and resemblance to the upper Draupne shale in well 15/3-8.

Figure 14: λ–μ–ρ crossplot showing data from Tau and Draupne formations in six immature to early mature wells and one mature well (15/3-8 upper and lower shale). The black arrow indicates the inorganic background shale compaction trend. (a) Color coded by well number. (b) Color coded with TOC. (c) Color coded with resistivity. For reference to the V_p/V_s–AI domain, see Figure 10.

Figure 15: Modeled AVO signature from synthetic seismic based on well log data (0–30°). Location of wells (a) corresponds to color of signature in R_{pp}–θ plot (b) and per-well

For Peer Review

background trends in the Intercept–Gradient (I–G) plot (c). I–G plots are sorted according to increasing depth of source rock encounter from top to bottom. 3 m and 10 m blocking intervals are represented by grey and black points, respectively.

Figure 16: Well correlation between 15/12-3, 15/12-23 and 15/12-22 in the southwest Ling Depression. Draupne Formation indicated with black shading. The logs shown are gamma ray and resistivity-sonic overlay. Increasing separation caused by the resistivity log indicates higher maturity. Increasing separation caused by the sonic log represents higher TOC.

Figure 17: Schematic interpretation of V_p/V_s–AI trends based on our well log data, in relation to arbitrary constant-TOC lines indicating increasing compaction and maturation pre-oil generation. Average values are shown with error bars for variation, and average TOC at each well location is denoted. Inferred relative changes for a given shale point is illustrated in the top right. The TOC trend is supported by kerogen substitution, the compaction trend is based on increasing depth of shale formations, and the hydrocarbon trend is inferred to explain the additional reduction of V_p/V_s and AI in mature shale, supported by fluid substitution.

For Peer Review

LIST OF TABLES

For Peer Review

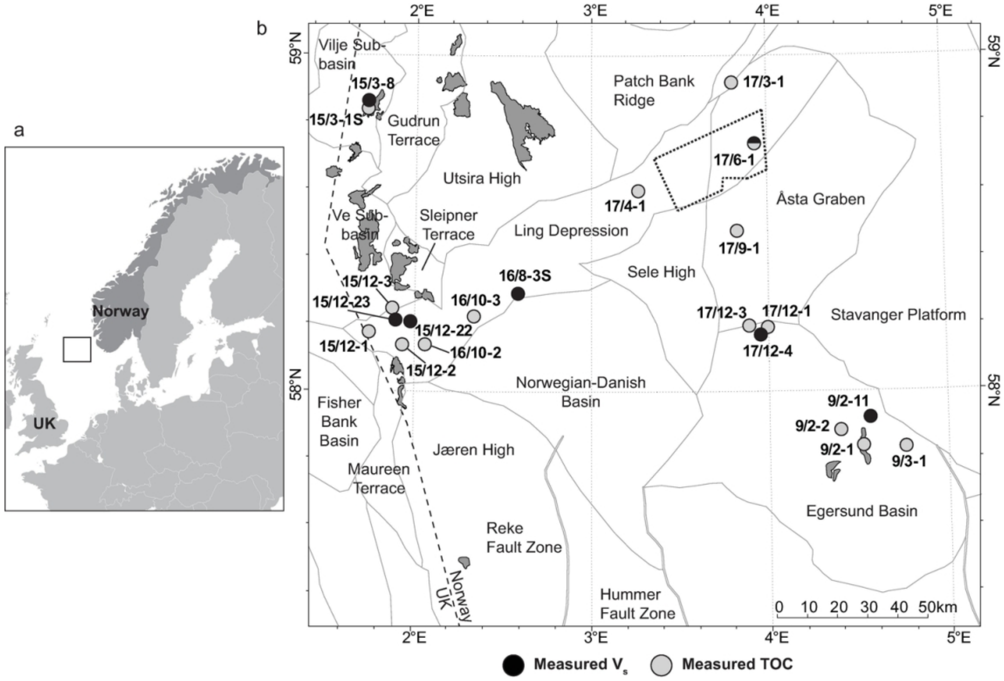

Figure 1: (a) Overview map showing location of the study area. (b) Detail view of the study area showing Central North Sea structural elements (NPD, 2017) and wells included in the database. Producing fields (presently or in the past) are marked with grey shading. The TA0701 3D seismic survey is outlined with a stippled rectangle.

120x81mm (300 x 300 DPI)

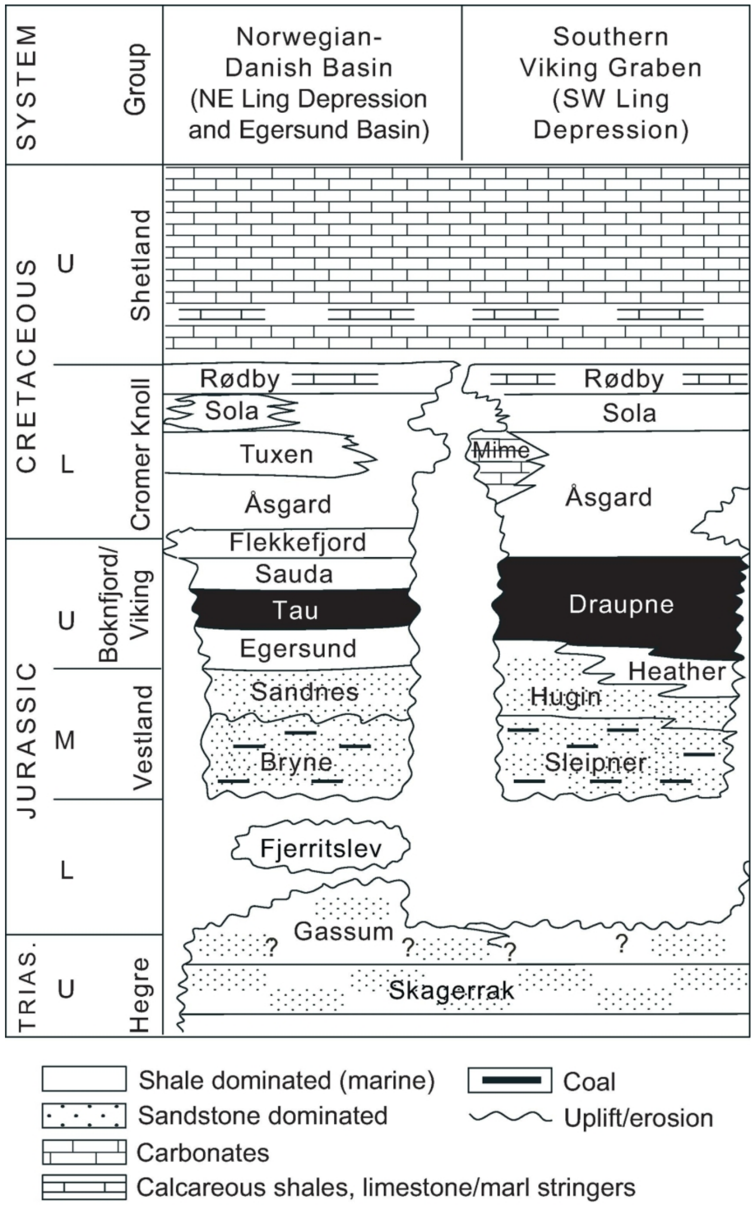

Figure 2: Generalized Mesozoic stratigraphic succession in the study area (modified from NPD, 2014).

130x210mm (300 x 300 DPI)

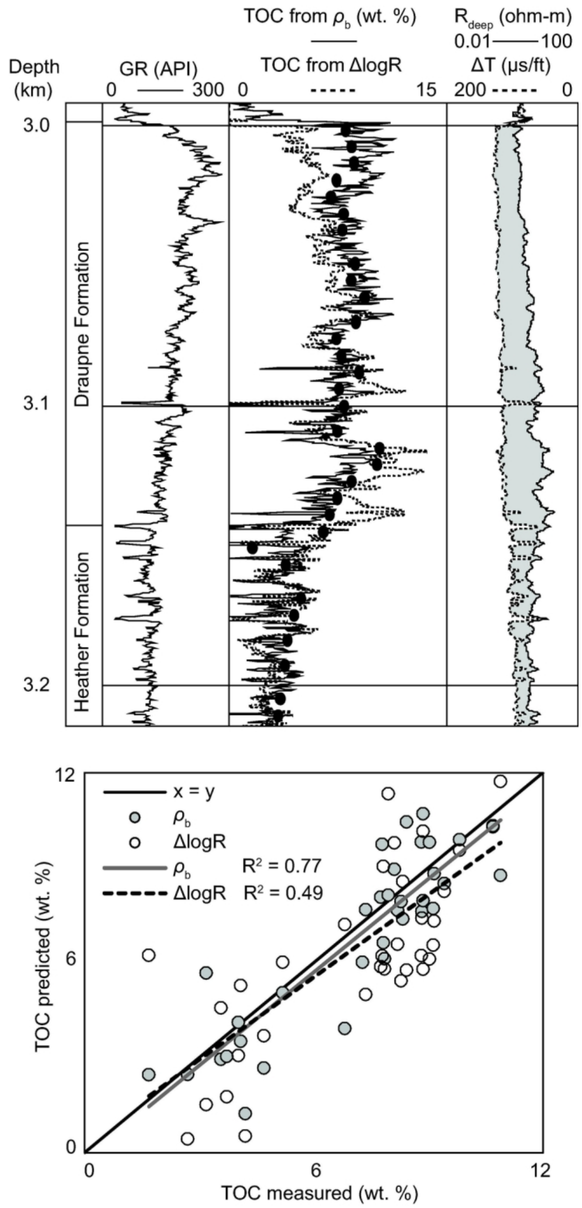

Figure 3: Comparison of TOC calculated from the ΔlogR method (Passey et al., 1990; dotted line) and from bulk density through equation 1 (solid line), with measured TOC (black dots) in calibration well 15/12-3. Gamma ray is shown to the left and resistivity-sonic overlay to the right. A crossplot of predicted versus measured TOC is shown below.

83x174mm (300 x 300 DPI)

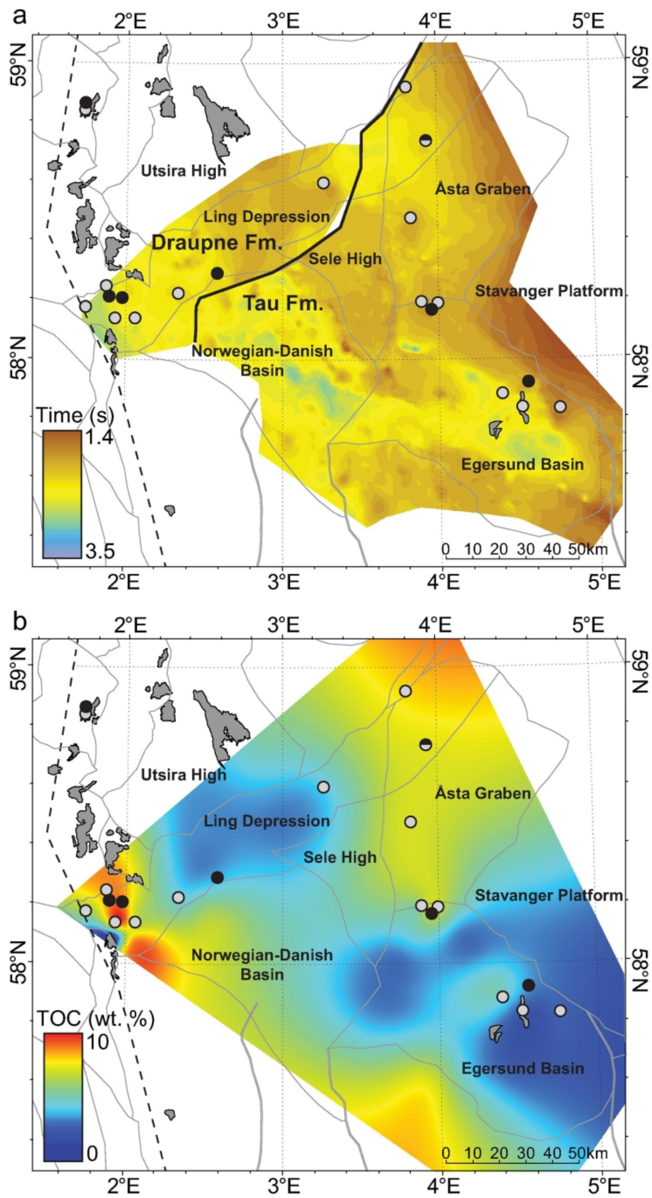

Figure 4: (a) Two way time (TWT) map of top Tau and Draupne formations from available 2D seismic data. (b) TOC distribution based on well data points (average per well). Note that the map is based on all locations with geochemical data in the area, but only wells included in our main database are shown for reference.

156x290mm (300 x 300 DPI)

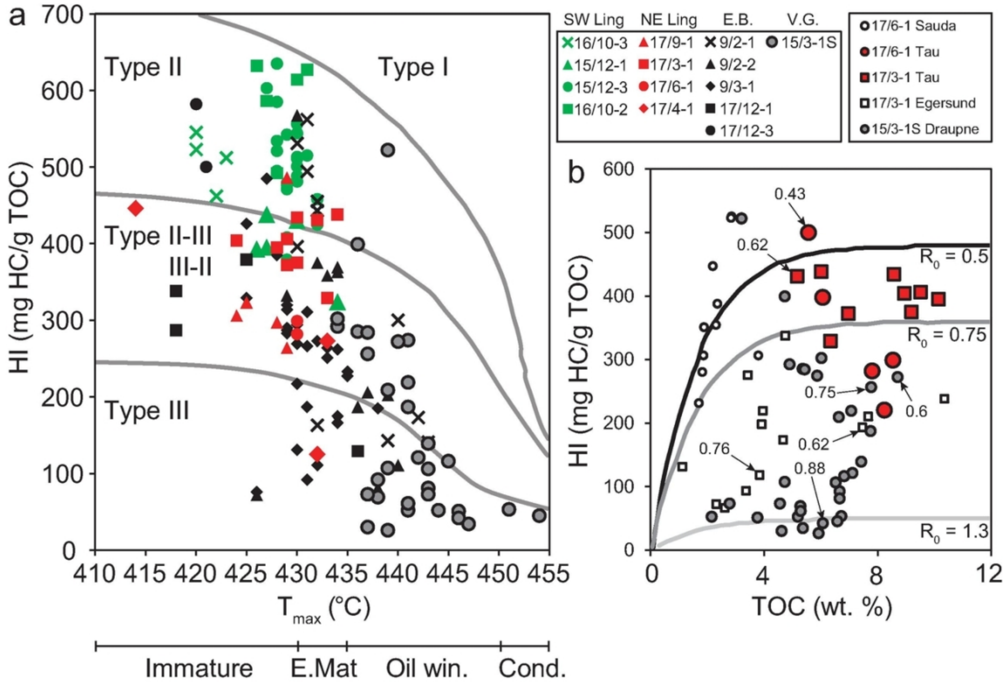

Figure 5: (a) T_{max} versus HI plot used as a kerogen type and thermal maturity indicator (Isaksen and Ledje, 2001). Green points are from southwest Ling Depression, red points from northeast Ling Depression and Åsta Graben, and black points are from the Egersund Basin (E.B.). Grey points are from the mature southern Viking Graben reference area (V.G.). (b) TOC versus HI for well 15/3-1S, 17/6-1 and 17/3-1 (Sauda and Egersund formations for comparison). Also indicated are associated vitrinite reflectance readings and reference lines from Vernik and Landis (1996).

109x75mm (300 x 300 DPI)

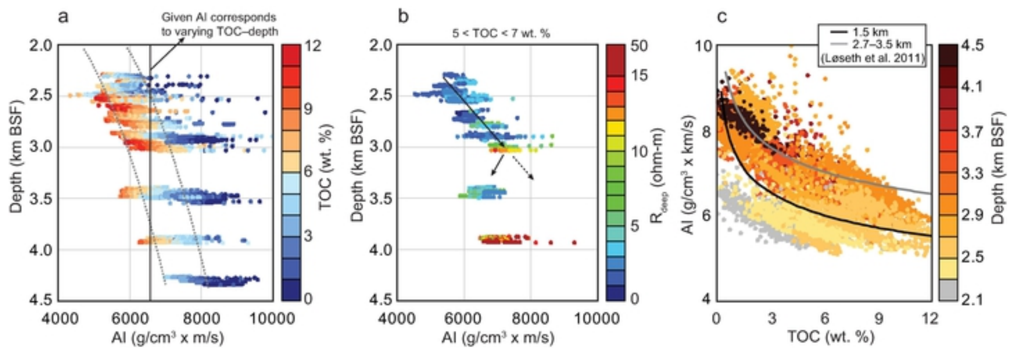

Figure 6: (a) AI versus depth with TOC color code. Stippled grey lines are adapted from Løseth et al. (2011). (b) AI versus depth with resistivity color code (data with 5 < TOC < 7 wt. %. (c) Comparison between AI–TOC trends from Løseth et al. (2011) and data from the study area, color coded with depth.

61x20mm (300 x 300 DPI)

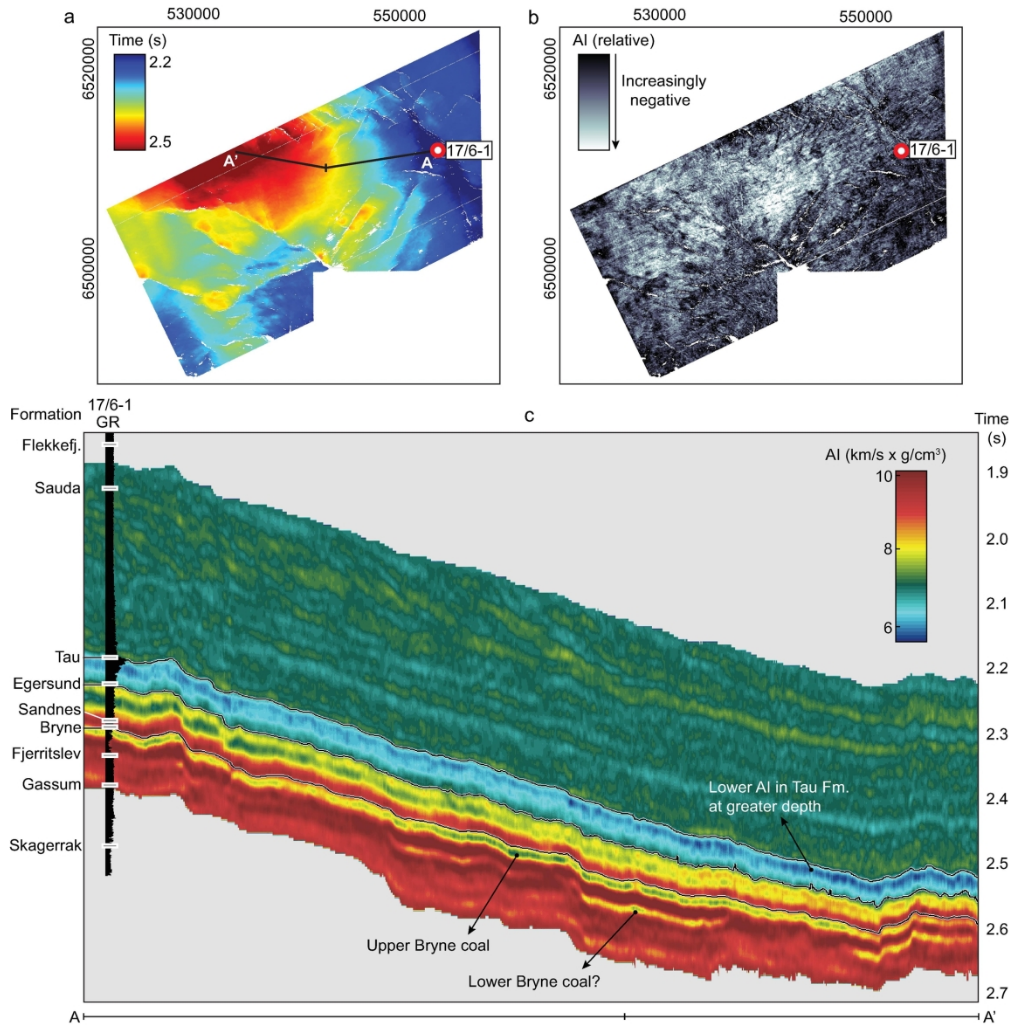

Figure 7: (a) Map of top Tau Formation in TWT (s) based on 3D seismic data outlined in Figure 1, with location of arbitrary line A–A′. (b) Relative AI extracted 5 ms below the top Tau reflector showing relatively increasing contrast to the layer above towards deeper part of basin. Position of well 17/6-1 is indicated by the red point. (c) Inverted AI displayed along line A–A′. Top Tau, top Egersund and top Bryne horizons are shown for reference along with gamma ray log and formation tops in well 17/6-1.

180x185mm (300 x 300 DPI)

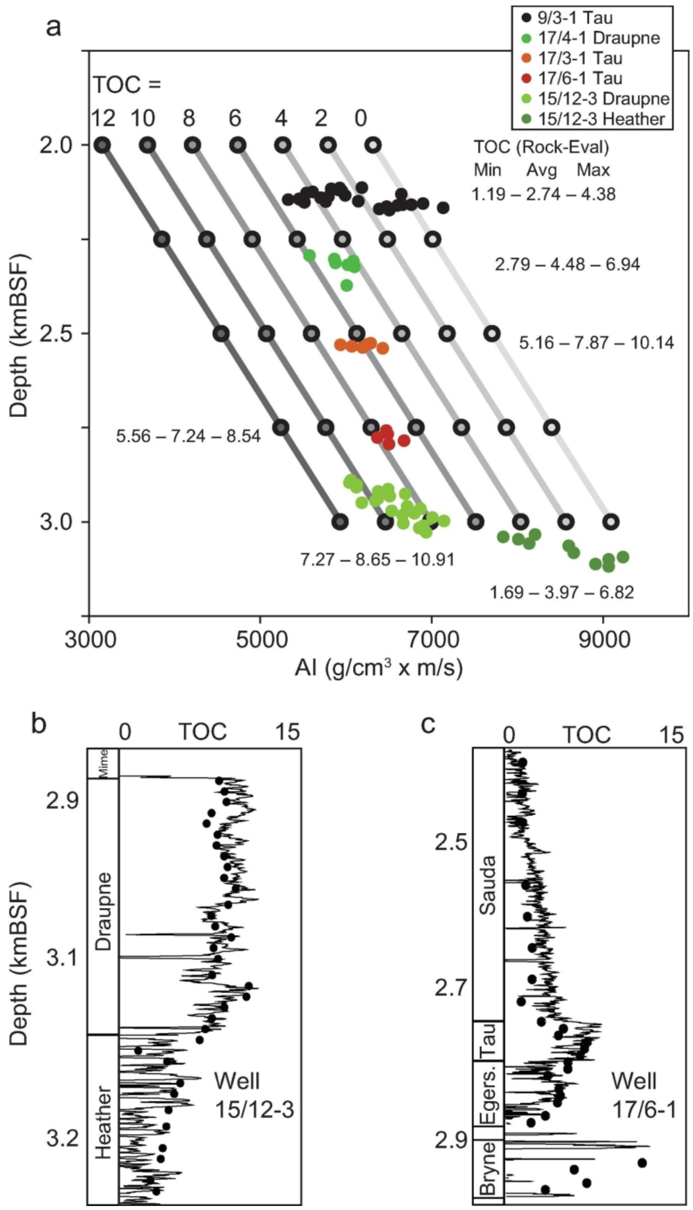

Figure 8: (a) Realizations of equation 3, relating AI and depth (below sea floor, corrected for exhumation) to TOC, superimposed on data from organic-rich shale intervals in five wells. TOC predicted from equation 3 is shown in well 15/12-3 (b) and well 17/6-1 (c) compared to TOC from Rock-Eval (black points).

141x244mm (300 x 300 DPI)

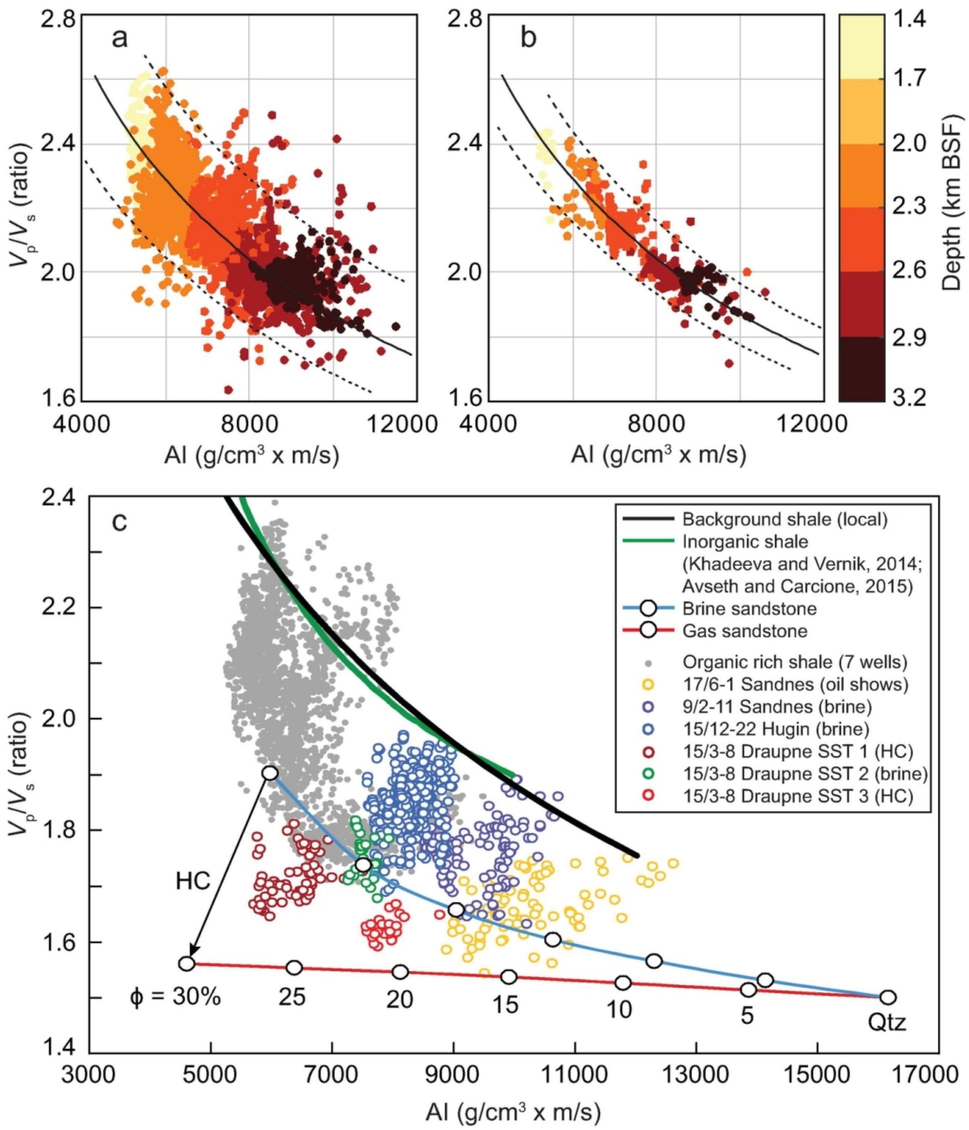

Figure 9: V_p/V_s–AI crossplot color coded with depth (km BSF) corrected for exhumation, showing background non-organic shales with (a) recorded well log scale and (b) ~3 m upscaling. The fitted black line corresponds with expected compaction behavior in this domain. Dotted lines indicate approximate range between maximum and minimum values. (c) Calibration of V_p/V_s–AI sandstone trends to data from the study area. Source rock shale data are shown as grey points, and the empirical background shale trend and a published inorganic shale trend are included for reference (Khadeeva and Vernik, 2014; Avseth and Carcione, 2015).

127x143mm (300 x 300 DPI)

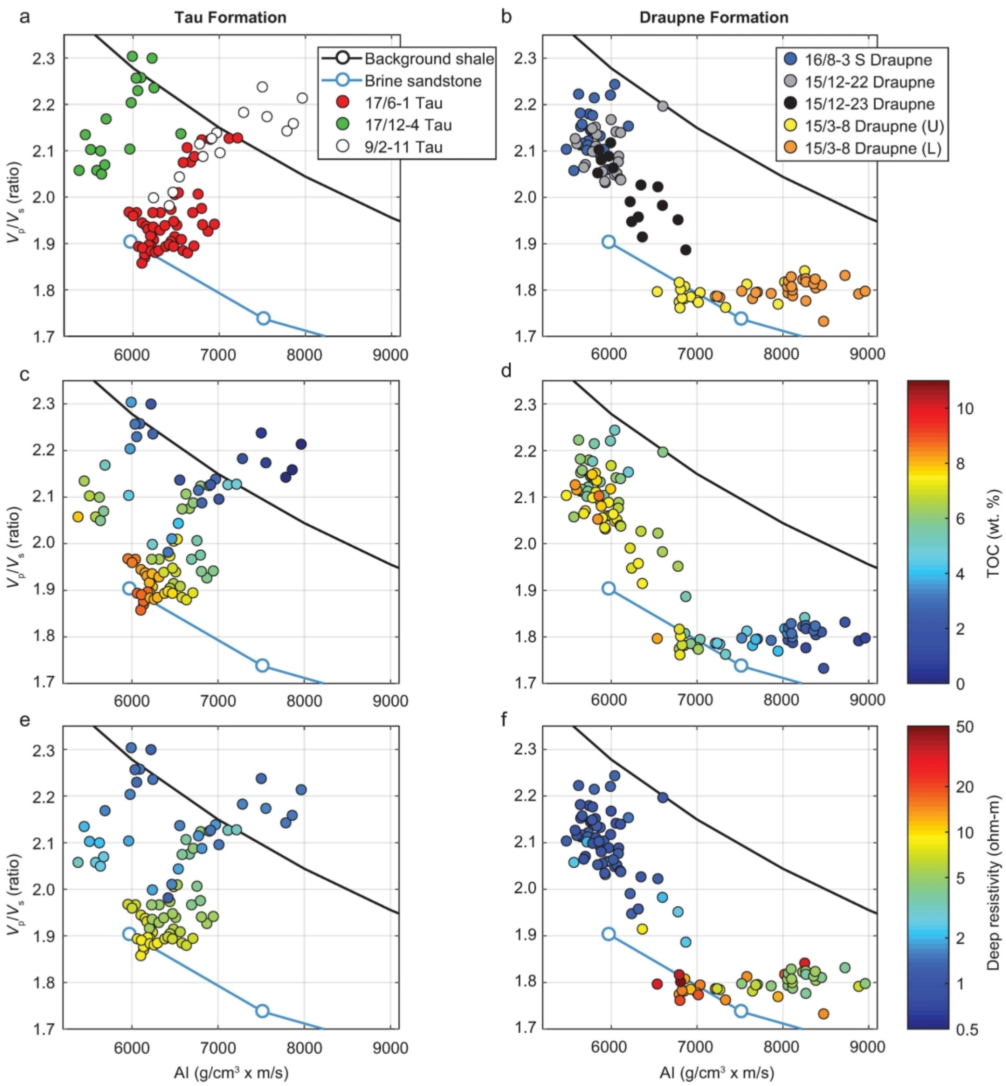

Figure 10: Organic rich shale formations (Tau and Draupne in left and right column, respectively) plotted on V_p/V_S–AI RPT calibrated to the study area, upscaled data. Color code represents well number (a, b), TOC (c, d) and deep resistivity (e, f).

187x201mm (300 x 300 DPI)

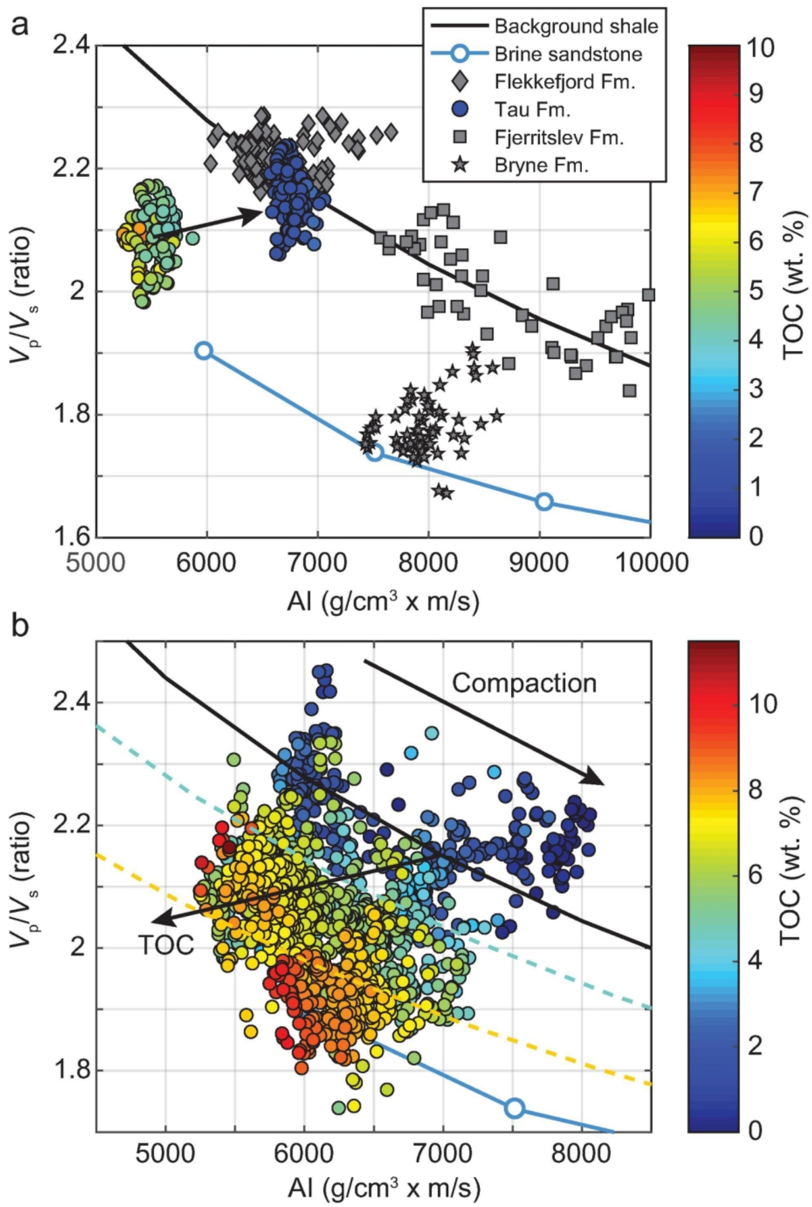

Figure 11: (a) Comparison between the Tau Formation (well 17/12-4) in situ (4 < TOC < 7 wt. %) and after kerogen substitution in the V_p/V_s–AI plot, shown with shallower and deeper organic lean shales (Flekkefjord and Fjerritslev formations, respectively) and brine sandstone (Bryne Formation). (b) V_p/V_s–AI data from the source rock intervals in six wells within immature to early mature stages. Shifted compaction trends coarsely capture increasing TOC in data on the well log scale.

123x183mm (300 x 300 DPI)

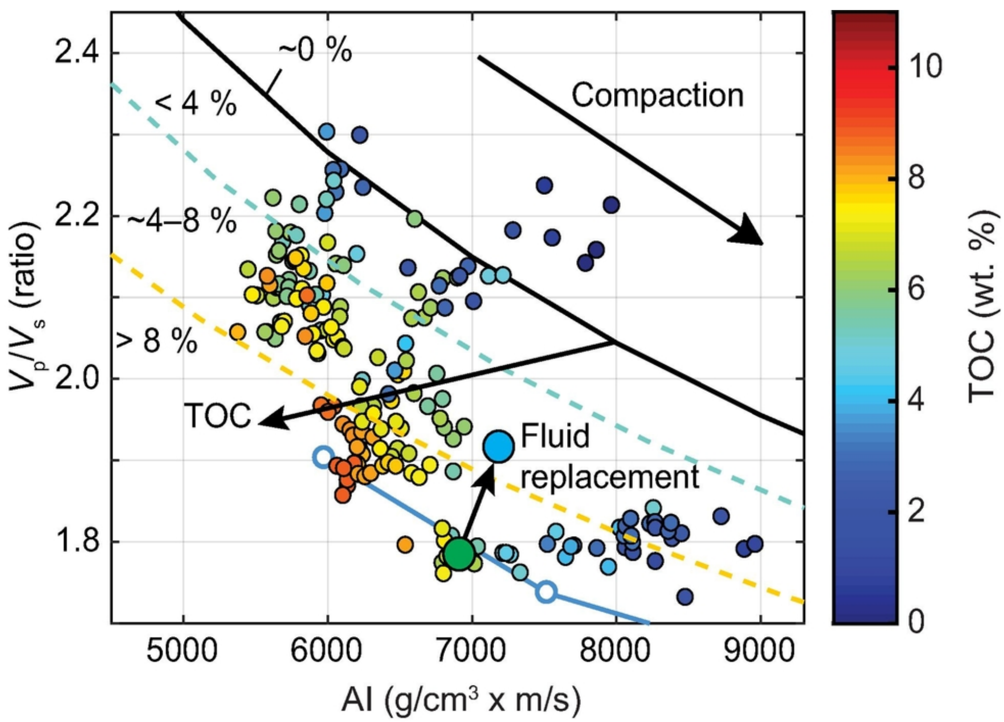

Figure 12: Upscaled data from seven wells superimposed on "constant-TOC" compaction lines, color coded with TOC. Replacing in-situ oil (green) with brine (blue) in the upper Draupne shale (well 15/3-8) is expressed with average V_p/V_s and AI before and after fluid substitution. Notice that the brine-scenario shows improved coherence with the TOC trendlines.

82x59mm (300 x 300 DPI)

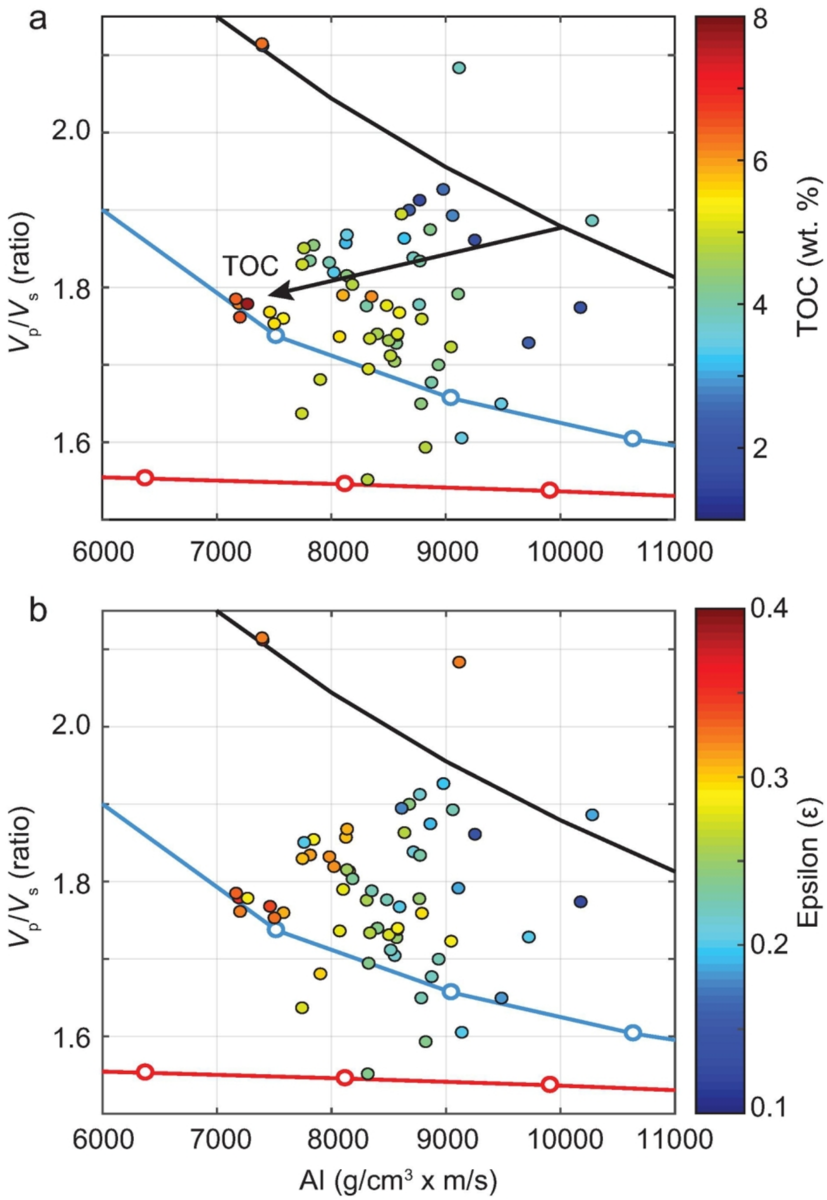

Figure 13: Ultrasonic measurements from Sondergeld et al. (2000) expressed in the V_p/V_s-AI crossplot with color code according to (a) TOC and (b) P-wave anisotropy expressed by epsilon (ε). Notice overall similar trend in TOC as described in well log data, and resemblance to the upper Draupne shale in well 15/3-8.

120x175mm (300 x 300 DPI)

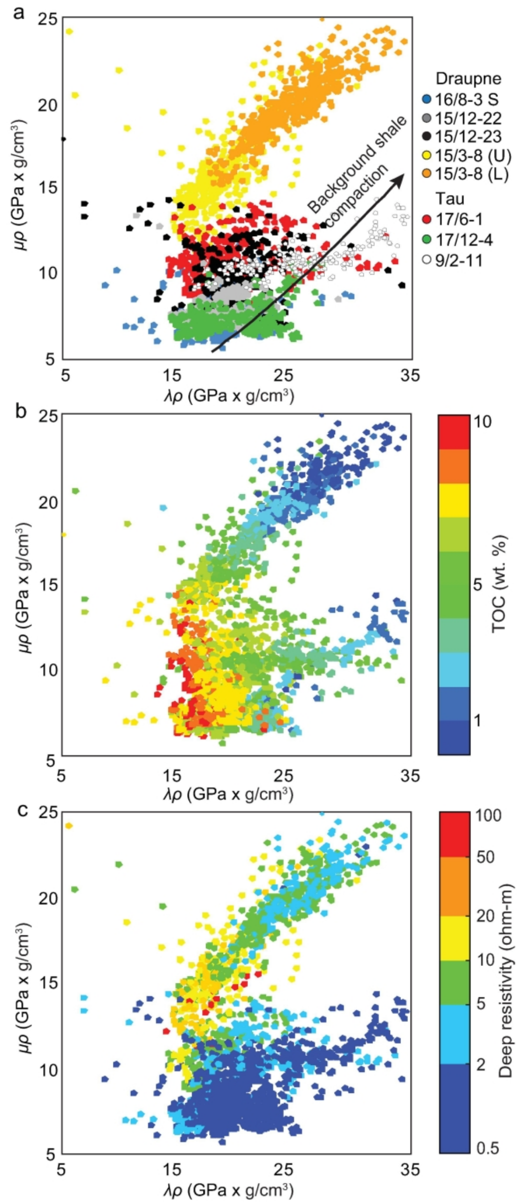

Figure 14: λ–μ–ρ crossplot showing data from Tau and Draupne formations in six immature to early mature wells and one mature well (15/3-8 upper and lower shale). The black arrow indicates the inorganic background shale compaction trend. (a) Color coded by well number. (b) Color coded with TOC. (c) Color coded with resistivity. For reference to the V_p/V_S–AI domain, see Figure 10.

196x459mm (300 x 300 DPI)

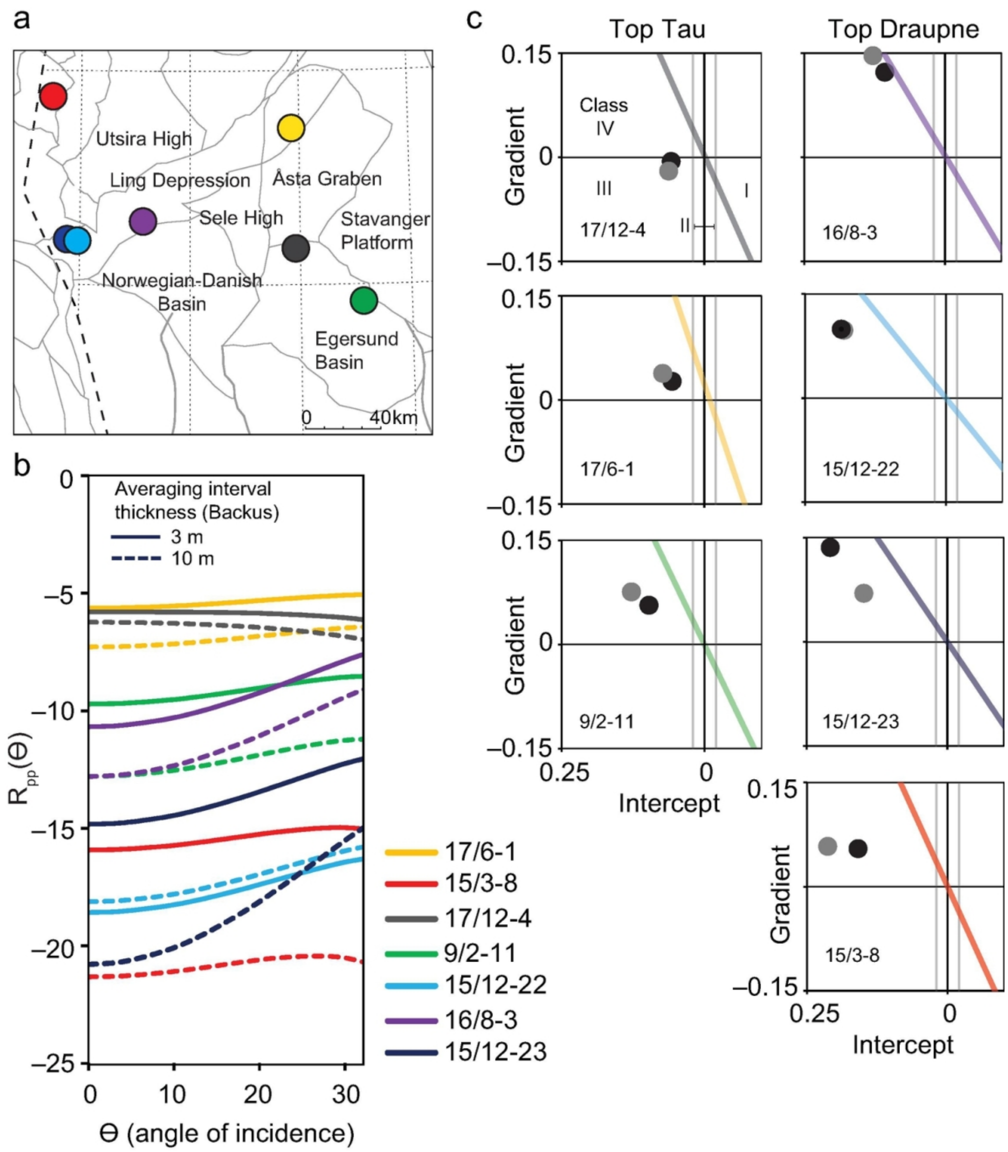

Figure 15: Modeled AVO signature from synthetic seismic based on well log data (0–30°). Location of wells (a) corresponds to color of signature in R_{pp}–θ plot (b) and per-well background trends in the Intercept–Gradient (I–G) plot (c). I–G plots are sorted according to increasing depth of source rock encounter from top to bottom. 3 m and 10 m blocking intervals are represented by grey and black points, respectively.

124x143mm (300 x 300 DPI)

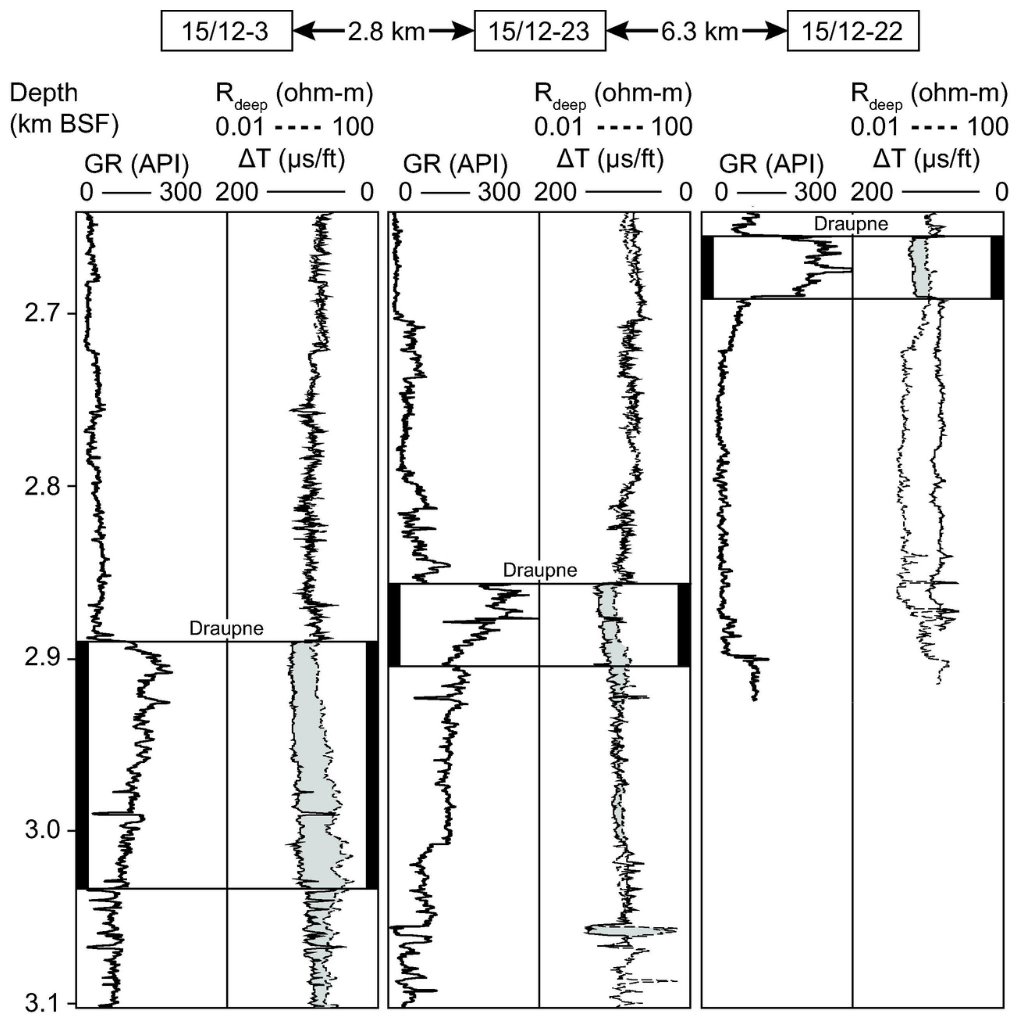

Well correlation between 15/12-3, 15/12-23 and 15/12-22 in the southwest Ling Depression. Draupne Formation indicated with black shading. The logs shown are gamma ray and resistivity-sonic overlay. Increasing separation caused by the resistivity log indicates higher maturity. Increasing separation caused by the sonic log represents higher TOC.

108x109mm (300 x 300 DPI)

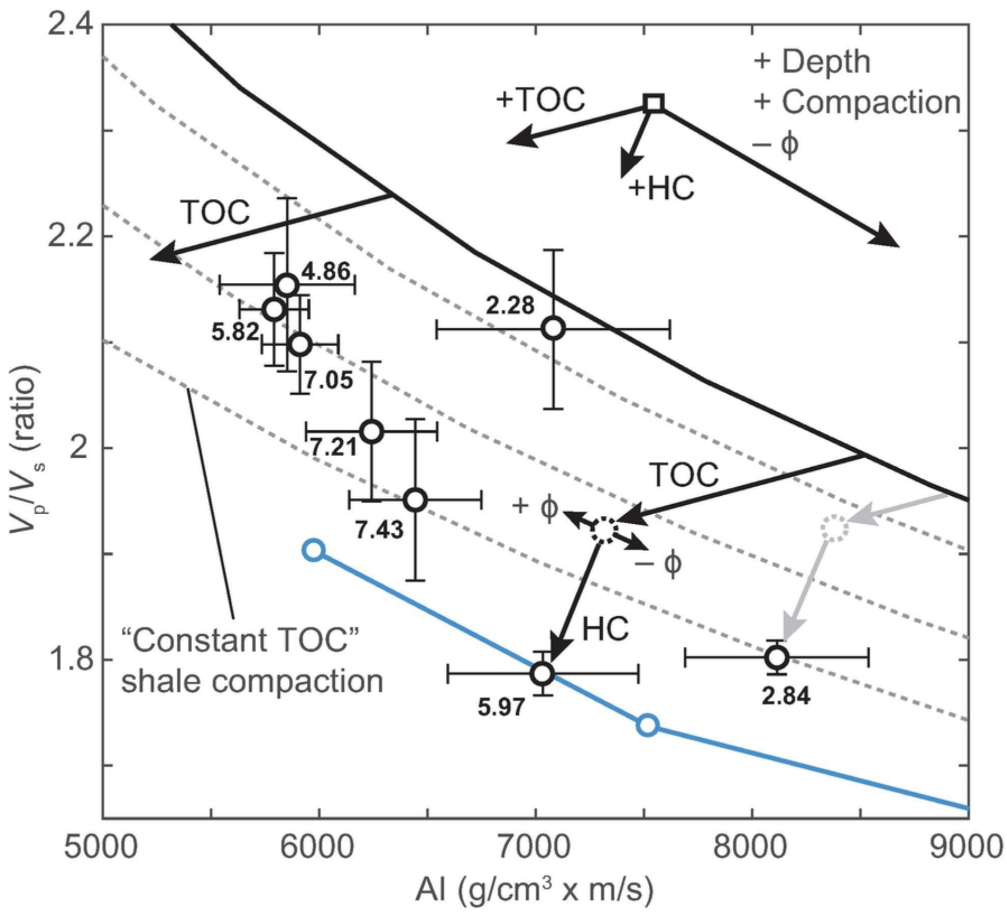

Figure 17: Schematic interpretation of V_p/V_s–AI trends based on our well log data, in relation to arbitrary constant-TOC lines indicating increasing compaction and maturation pre-oil generation. Average values are shown with error bars for variation, and average TOC at each well location is denoted. Inferred relative changes for a given shale point is illustrated in the top right. The TOC trend is supported by kerogen substitution, the compaction trend is based on increasing depth of shale formations, and the hydrocarbon trend is inferred to explain the additional reduction of V_p/V_s and AI in mature shale, supported by fluid substitution.

75x68mm (300 x 300 DPI)

Table 1: Depth and thickness of the Tau and Draupne formations encountered in the selected well database. The presence of measured shear velocity is indicated in the last column.

Formation	Well #	Formation top depth [m BSF] Present	Max.*	Thickness [m]	V_s
Tau	17/6-1 (Svaneøgle)	2198	2748	54	✓
	17/3-1 (Bark)	2013	2513	28	✗
	17/9-1	1997	2497	40	✗
	17/12-4	2021	2421	49	✓
	17/12-1 (Vette)	2025	2450	47	✗
	17/12-3	2100	2475	51	✗
	9/2-11 (Aubrey)	2365	2865	82	✓
	9/2-1 (Yme)	2865	3505	104	✗
	9/2-2	2835	3485	105	✗
	9/3-1	1561	2111	64	✗
Draupne	17/4-1	1990	2290	96	✗
	16/8-3 S (Lupin)	2473	2623	86	✓
	16/10-2	2713	2713	36	✗
	16/10-3	2386	2586	20	✗
	15/12-22 (Storkollen)	2656	2656	35	✓
	15/12-23	2853	2853	47	✓
	15/12-1	2886	2886	21	✗
	15/12-2	2592	2592	61	✗
	15/12-3	2886	2886	145	✗
	15/3-8 (U)	3873	3873	57	✓
	15/3-8 (L)	4262	4262	78	✓
	15/3-1 S (Gudrun)	3813	3813	807	✗

* Corrected for estimated exhumation to represent maximum burial depth

For Peer Review

Table 2: Summary of TOC and vitrinite reflectance from available well reports (NPD, 2017). TOC predicted from Equation 1 is included for comparison in all wells.

		TOC [wt. %] Rock-Eval		TOC [wt. %] Log*		R_o [%]		
Formation	Well no. (Prospect)	μ†	σ†	μ	σ	n†	μ	σ
Tau	17/6-1 (Svaneøgle)	7.2	1.2	7.4	1.2	21	0.43	0.06
	17/3-1 (Bark)	7.9	1.7	7.4	2.0	30	0.62	0.04
	17/9-1	7.0	1.9	7.5	3.6	–	–	–
	17/12-4	–	–	4.9	2.0	–	–	–
	17/12-1 (Vette)	6.8	2.3	6.1	1.9	16	0.44	?
						14	0.49	?
	17/12-3	5.6	1.6	5.6	0.7	21	0.38	?
						8	0.45	?
	9/2-11 (Aubrey)	–	–	2.3	1.8	–	–	–
	9/2-1 (Yme)	2.4	1.2	2.7	2.1	20	0.46	0.06
	9/2-2	4.4	2.2	4.4	2.2	4	0.53	0.08
						11	0.55	0.04
						9	0.58	0.05
						3	0.61	0.03
	9/3-1	2.7	0.9	2.3	1.5	–	–	–
Draupne	17/4-1	4.2	1.7	4.6	1.5	–	–	–
	16/8-3 S (Lupin)	–	–	5.8	0.8	–	–	–
	16/10-2	6.4	1.5	6.2	1.5	12	0.47	0.04
						9	0.52	0.05
	16/10-3	4.6	2.2	4.3	2.3	23	0.43	?
	15/12-22 (Storkollen)	–	–	7.1	1.4	–	–	–
	15/12-23	–	–	7.2	1.0	–	–	–
	15/12-1	6.2	0.3	6.5	1.9	19	0.47	0.04
	15/12-2	9.6	0.8	9.3	1.7	–	–	–
	15/12-3	8.7	1.0	8.3	1.7	1	0.39	–
						16	0.43	0.04
						12	0.47	0.04
	15/3-8 (U)	–	–	6.0	1.4	–	–	–
	15/3-8 (L)	–	–	2.8	1.2	–	–	–
	15/3-1 S (Gudrun)	5.8	1.5	5.4	1.5	20	0.60	0.09
						5	0.63	0.04
						17	0.68	0.08
						20	0.75	0.07
						3	0.88	0.02

* Predicted from ρ_b–TOC relation (Equation 1)

† μ = mean; σ = standard deviation; n = number of readings

For Peer Review